POLITECNICO DI TORINO
Repository ISTITUZIONALE

A 3D-1D virtual element method for modeling root water uptake

Original
A 3D-1D virtual element method for modeling root water uptake / Berrone, S., Ferraris, S., Grappein, D., Teora, G., Vicini, F.. - In: COMPUTERS & MATHEMATICS WITH APPLICATIONS. - ISSN 0898-1221. - 213:(2026), pp. 22-52. [10.1016/j.camwa.2026.03.027]

Availability:
This version is available at: 11583/3009633 since: 2026-04-07T07:04:53Z

Publisher:
Elsevier

Published
DOI:10.1016/j.camwa.2026.03.027

Terms of use:

This article is made available under terms and conditions as specified in the corresponding bibliographic description in the repository

Publisher copyright

(Article begins on next page)

18 November 2026

Computers and Mathematics with Applications 213 (2026) 22–52

Contents lists available at ScienceDirect

Computers and Mathematics with Applications

journal homepage: www.elsevier.com/locate/camwa

A 3D-1D virtual element method for modeling root water uptake

Stefano Berrone [a,b], Stefano Ferraris [c], Denise Grappein [d,b], Gioana Teora [a,b,*], Fabio Vicini [a,b]

[a] Dipartimento di Scienze Matematiche "G. L. Lagrange", Politecnico di Torino, Corso Duca degli Abruzzi, 24, Torino, 10129, Italy
[b] Members of INdAM-GNCS group, Italy
[c] Dipartimento Interateneo di Scienze, Progetto e Politiche del Territorio, Politecnico di Torino e Università di Torino, Viale Mattioli, 39, Castello del Valentino, 10125, Torino, Italy
[d] Istituto Nazionale di Alta Matematica "F. Severi", Piazzale Aldo Moro 5 00185, Roma, Italy

ARTICLE INFO

2020 MSC:
65N30
35K55
65M60

Keywords:
Optimization
Soil-roots
Coupling
Virtual element method

ABSTRACT

We present a novel optimization-based strategy to simulate soil-root interactions and predict water uptake during the growth of a root system. By rigorously reducing the coupled Richards-Stokes problem to a well-posed 3D-1D formulation, we solve it in a PDE-constrained optimization framework, enabling a direct quantification of root water uptake. To address the non-linearity of the 3D Richards equation and the coupling with the 1D variables, we propose a tailored solving strategy that ensures an accurate and efficient approximation of the solutions. For the first time, the Virtual Element Method is employed to discretize the three-dimensional soil sample, significantly enhancing the method's capacity to handle complex geometries. Indeed, this enables efficient meshing of domains containing stones and other impervious obstacles of arbitrary shapes. Several numerical examples are provided, showcasing the accuracy of the method and demonstrating its applicability both on static and dynamic root systems.

1. Introduction

In recent years, the study of the interactions between root system architecture (RSA) and soil has gained significant interest, in particular in the framework of actions confronting climate change and drought, the management of water resources, and the reinforcement of the soil stability [1–6]. However, investigating root activities and architecture during growth in situ can be very expensive and challenging, as the involved processes are often very slow and the RSA usually exhibits considerable variability even within the same species and under identical environmental conditions. Therefore, modeling root water potential and uptake in various 3D soil geometries is crucial, for instance, for guiding the design of experimental measurements that support nature-based solutions to mitigate shallow landslides, restore natural ecosystems and enhance water use efficiency in agriculture [7–9].

In this paper, we aim at modeling water flow in unsaturated soil and within the root xylem, i.e. the tissue responsible for distributing the water absorbed from the soil, to estimate the root water uptake. This process occurs while the RSA dynamically expands over time, influenced by soil variables such as pressure head and water content. The water flow is governed by the non-linear, time-dependent Richards equation in the unsaturated soil and by a Stokes-like equation accounting for frictional forces in the xylem. We first reduce the coupled 3D-3D Richards-Stokes system to a well-posed 3D-1D problem by making some assumptions on the RSA and on the regularity of the solution. Proper subspaces of the classical Sobolev spaces are defined to be used in the variational formulation

* Corresponding author.
E-mail address: gioana.teora@polito.it (G. Teora).

https://doi.org/10.1016/j.camwa.2026.03.027
Received 19 February 2025; Received in revised form 20 March 2026; Accepted 25 March 2026
Available online 6 April 2026
0898-1221/© 2026 The Author(s). Published by Elsevier Ltd. This is an open access article under the CC BY-NC-ND license (http://creativecommons.org/licenses/by-nc-nd/4.0/).

of partial differential equations. The reduction of the 3D Stokes equation with friction in the xylem results in a Darcy equation in mixed form, requiring the definition of suitable subspaces for both xylem velocity and pressure variables. Finally, we devise a tailored optimization strategy to solve the arising reduced non-linear problem, enabling the simulation of dynamic RSA and providing a direct quantification of water uptake from interface variables, without requiring any post-processing operations.

We employ the Virtual Element Method (VEM) for the discretization of the 3D pressure head. This method is a Galerkin approximation method that extends the Finite Element Method to polytopal meshes [10,11]. To the best of our knowledge, for the first time, the viability of the VEM is tested in the numerical resolution of the Richards equation in its primal form. Previously, VEM was applied only to the mixed form of the two-dimensional Richards equation in [12], where convergence estimates for the lowest-order formulation, based on the Kirchhoff transformation, were derived. The adoption of VEM for soil discretization significantly enhances the method's flexibility to naturally handle general polyhedral meshes, including elements with aligned edges and faces, as well as concave polyhedra. This capability is particularly advantageous for meshing and simulating scenarios characterized by complex geometries arising from obstacles, physical barriers, or layered and fractured soil [13,14]. Additionally, VEM simplifies the representation of irregularly shaped domains, such as plant pots [15] or locally refined grids [16,17], making it especially well-suited for modeling intricate and heterogeneous environments.

A mixed Finite Element formulation with a strong imposition of continuous pressure and flux conservation at root branching points is adopted for the xylem variables.

In the numerical experiments, root growth is modeled by means of a continuous-discrete hybrid tip-tracking strategy, in which the growth direction and the formation of branches depend both on environmental conditions and on plant genetics [15,18–22]. Notably, to avoid root tip intrusion into impenetrable regions, we introduce a scalar field that steers the root tip away from the barrier surface. This field is defined only outside the obstacle, within a narrow neighborhood, and facilitates the reproduction of the negative thigmotropic response of plant roots. This approach does not require iterative corrections of root tip positions [14] or the solution of equations inside the obstacles [8], limiting the computational effort. Indeed, obstacles are excluded from the computational domain thanks to the VEM, which enables a flexible discretization of the domain surrounding the obstacle even in the presence of complex or irregularly shaped barriers.

The method is tested on both static and dynamic root system architectures. Root properties, such as root age, are tracked during the simulations, enabling some problem coefficients to vary accordingly. The proposed experiments demonstrate the flexibility of the method in handling complex geometric configurations and confirm the efficiency of the iterative solving strategy employed to tackle non-linearities. In particular, when combined with an appropriate preconditioning strategy, the proposed approach proves to be a viable option to tackle simulations with an increasing number of degrees of freedom.

The outline of the paper is as follows. In Section 2, we present the 3D-3D coupled problem, while in Section 3, after performing the model reduction, we introduce the PDE-constrained optimization problem. In Section 4, we detail the time and space discretizations and describe our solving strategy to handle the arising non-linear problem through the conjugate gradient scheme. In Section 5, we detail how to account for the presence of physical barriers in our discrete model, whereas in Section 6, we propose some numerical experiments to validate and show the viability of our procedure. Details on the root growth used in the experiments are provided in Appendices A and B, whereas details on the matrices involved in the solving strategy are reported in Appendix C. The numerical and geometric tools used to carry out the experiments are available as open source in the *PolyDiM* library [23].

1.1. Notation

Given a generic Sobolev space $\mathcal{H}$, we use the symbol $\|\cdot\|_{\mathcal{H}}$ to indicate the norm in $\mathcal{H}$, and $(\cdot,\cdot)_{\mathcal{H}}$ to denote the scalar product in $\mathcal{H}$. When $\mathcal{H} = L^2(\omega)$, with ω a generic open subset $\omega \subset \mathbb{R}^d$, $d = 1, 2, 3$, we adopt a lighter notation, denoting by $(\cdot,\cdot)_\omega$ the scalar product in $L^2(\omega)$. Precisely, given two scalar functions $p, q \in L^2(\omega)$, two vector fields $\boldsymbol{a},\ \boldsymbol{v} \in \left[L^2(\omega)\right]^d$ and two tensor fields $\boldsymbol{T},\ \boldsymbol{\sigma} \in \left[L^2(\omega)\right]^{d\times d}$, we denote by

$$(p,q)_\omega = \int_\omega pq \ d\omega, \quad (\boldsymbol{a},\boldsymbol{v})_\omega = \int_\omega \boldsymbol{a}\cdot\boldsymbol{v} \ d\omega, \quad (\boldsymbol{T},\boldsymbol{\sigma})_\omega = \int_\omega \boldsymbol{T} : \boldsymbol{\sigma} \ d\omega,$$

where $\boldsymbol{T} : \boldsymbol{\sigma} := \sum_{i,j=1}^{n} \boldsymbol{T}_{ij}\boldsymbol{\sigma}_{ij}$.

Let us consider a finite time interval $(0, \bar{t}]$, i.e., $\bar{t} < +\infty$ and its discretization in J sub-intervals $\mathcal{I}_j = (t_{j-1}, t_j]$, where the instants t_j are such that

$$0 = t_0 < t_1 < \cdots < t_J = \bar{t}.$$

Let $\Omega \subset \mathbb{R}^3$ be a polyhedral convex domain representing the soil sample, and let $\Sigma(t_j) = \Sigma^j \subset \Omega$ denote the root system architecture which is considered fixed while the quantities of interest vary during the time interval $\mathcal{I}_j$. In the following, we assume that Σ^j is composed of thin tubular vessels of constant radius R, and that R is much smaller than the root length and the characteristic dimension of the domain Ω. Furthermore, we assume that

$$\Sigma^0 \subseteq \Sigma^1 \subseteq \cdots \subseteq \Sigma^J,$$

which means that we allow for the growth of the root network, but not for its regression or remodeling. The boundaries of Ω and Σ^j are denoted respectively by $\partial\Omega$ and $\partial\Sigma^j$. In particular,

$$\partial\Sigma^j = \Gamma^j \cup \partial\Sigma^j_{\text{tip}} \cup \partial\Sigma_{\text{collar}},$$

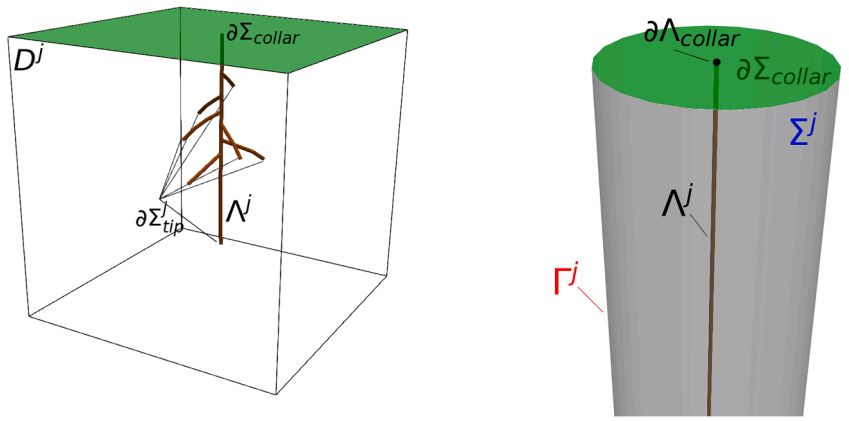


Fig. 1. Details on notation (zoom-in on the right).

where Γ^j denotes the lateral surface of the overall RSA, whereas $\partial\Sigma_{\text{collar}}$ and $\partial\Sigma^j_{\text{tip}}$ refer to the collar cross-section and to the union of the apical cross-sections (see Fig. 1). The root collar is defined as the interface between the stem and the roots and it is assumed to lie on the boundary of the soil-sample, i.e., $\partial\Sigma_{\text{collar}} \subset \partial\Omega$. The portion of soil not including the cylinder is denoted by $\mathcal{D}^j = \Omega \setminus \overline{\Sigma^j}$. We define $\partial\mathcal{D} \subset \partial\Omega$ as

$$\partial\mathcal{D} = \partial\Omega \setminus \partial\Sigma_{\text{collar}}. \tag{1}$$

Let us remark that $\partial\mathcal{D}$ and $\partial\Sigma_{\text{collar}}$ do not vary in time, hence we do not add the superscript j to these symbols. Finally, we denote by Λ^j the centerline of Σ^j, and we denote by $\partial\Lambda_{\text{collar}}$ the center of the collar cross-section and by $\partial\Lambda^j_{\text{tip}}$ the union of the centers of the apical cross-sections, such that $\overline{\Lambda^j} = \Lambda^j \cup \partial\Lambda_{\text{collar}} \cup \partial\Lambda^j_{\text{tip}}$.

2. The 3D-3D model

In the present section, we assume, for clarity of exposition, that Σ^j is made by a single straight cylindrical root segment. Details on how multiple segments are handled will be provided in Section 3.2.

The process of water uptake during the growth of the RSA is here described by means of two partial differential equations for the modeling of water flow in the soil sample and in the xylem, and an ordinary differential equation, modeling the evolution of the position of root tips.

In what follows, the subscript ς is used to refer to soil variables, while the subscript χ denotes xylem variables.

2.1. Water flow in soil

The soil water flux $\boldsymbol{u}_\varsigma$ is described by the Darcy law. This equation, combined with mass conservation, leads to the Richards equation, which models the flow of a wetting fluid (the water) in the unsaturated soil, under the effect of gravity and capillary action, and in the presence of a nonwetting fluid (the air) which is supposed to be at constant pressure equal to 0. The Richards equation at each time $t \in \mathcal{I}_j$, for $j = 1, \dots, J$, can be stated in the so-called head-based form as the non-linear, time-dependent, possibly degenerate, parabolic problem [24]

$$\begin{cases} \boldsymbol{u}_\varsigma = -K(\psi_\varsigma)\nabla[\psi_\varsigma + z] & \text{in } \mathcal{D}^j, \\ C(\psi_\varsigma)\frac{\partial\psi_\varsigma}{\partial t} + \operatorname{div}\boldsymbol{u}_\varsigma = 0 & \text{in } \mathcal{D}^j, \\ \psi_\varsigma = 0 & \text{on } \partial\mathcal{D}. \end{cases} \tag{2}$$

The symbol ψ_ς denotes the soil pressure head, which is positive in the saturated zone, where only water is present, and negative in the unsaturated zone. The symbol z denotes the vertical coordinate with the z-axis direction $\boldsymbol{e}_z$ oriented against the gravity direction, $K(\psi_\varsigma) = K(\theta(\psi_\varsigma))$ is the hydraulic conductivity, $\theta(\psi_\varsigma)$ is the volumetric soil-water content and $C(\psi_\varsigma) = C(\theta(\psi_\varsigma)) = \frac{d\theta}{d\psi_\varsigma}$ is the specific soil moisture capacity. In $\mathcal{I}_1 = (t_0, t_1]$, we define an initial condition in t_0

$$\psi_\varsigma = g_{\varsigma,0}, \quad \text{in } \mathcal{D}^0, \tag{3}$$

while, for $\mathcal{I}_j = (t_{j-1}, t_j]$ with $j \geq 2$, the pressure head at time t_{j-1} is directly provided by the value obtained at the end of the previous time interval.

Here, for the sake of clarity, we assume homogeneous Dirichlet boundary conditions for the soil pressure head, but other boundary conditions can be considered for Problem (2) to take into account natural phenomena like rainfall, snowmelt, runoff, and soil evaporation, as well as to prescribe fluxes along seepage faces or drainage boundaries [25].

The soil water content θ and, consequently, the hydraulic conductivity K and the capacity term C are modeled as a function of the soil pressure head ψ_ς using different characteristic curves which are usually determined experimentally for the different soils, as the van Genuchten's model [26]. Let us remark that the Richards equation degenerates into an elliptic equation if $C(\psi_\varsigma) = 0$ at some points of the domain. On the other hand, if $K(\psi_\varsigma) = 0$, then the equation becomes a first-order ordinary differential equation. Non-linearities and degeneracy pose significant challenges when dealing with this kind of problem [27]. Here, we consider the non-degenerate case and we assume that data are sufficiently regular.

2.2. Water flow in roots

Water transport in the xylem is modeled using the Stokes equations for incompressible Newtonian fluids [28,29], with the addition of a reactive term representing frictional forces to account for the porous nature of the xylem tissue. This leads to a Brinkman-like formulation of the flow problem [30], which can be written as:

$$\begin{cases} -\mathrm{div}\boldsymbol{\sigma}_\chi + K_a \boldsymbol{u}_\chi = -\rho g \boldsymbol{e}_z & \text{in } \Sigma^j, \\ \mathrm{div}\boldsymbol{u}_\chi = 0 & \text{in } \Sigma^j, \\ \boldsymbol{\sigma}_\chi \boldsymbol{n}_\chi = \boldsymbol{0} & \text{on } \partial\Sigma_{\text{collar}} \cup \partial\Sigma^j_{\text{tip}}. \end{cases} \tag{4}$$

Here, $\boldsymbol{u}_\chi$ is the flow velocity in the xylem, K_a is the resistance coefficient due to friction, ρ is the fluid density, and g is the gravity acceleration. The tensor $\boldsymbol{\sigma}_\chi$ is the Cauchy pseudo-stress tensor, i.e.

$$\boldsymbol{\sigma}_\chi = -p_\chi \boldsymbol{I} + \overline{\nu}\nabla\boldsymbol{u}_\chi, \tag{5}$$

where p_χ is the water pressure, $\overline{\nu}$ is the dynamic viscosity, and $\boldsymbol{I} \in \mathbb{R}^{3\times3}$ is the identity tensor. We assume homogeneous Neumann boundary conditions, but non-homogeneous conditions can be considered to express, for instance, a non-zero transpiration rate at the root collar [31].

2.3. The coupled problem

The two problems (2) and (4) are coupled by imposing the following interface conditions at Γ^j [32,33], namely

$$\boldsymbol{u}_\varsigma \cdot \boldsymbol{n}_\varsigma = -\boldsymbol{u}_\chi \cdot \boldsymbol{n}_\chi = \mu(\psi_\varsigma - \psi_\chi) \quad \text{on } \Gamma^j, \tag{6}$$

$$\boldsymbol{u}_\chi \cdot \boldsymbol{\tau}^d = \boldsymbol{0}, \quad d = 1,2, \quad \text{on } \Gamma^j, \tag{7}$$

where $\psi_\chi = \frac{p_\chi}{\rho g}$ is the xylem pressure head, μ expresses the conductivity of the root wall, $\boldsymbol{n}_\varsigma$ is the unit outward normal vector to Γ^j directed from soil to root and $\boldsymbol{n}_\chi = -\boldsymbol{n}_\varsigma$, while $\boldsymbol{\tau}^d$, $d = 1,2$, are two unit tangential vectors to Γ^j, such that

$$\boldsymbol{n}_\chi \boldsymbol{n}_\chi^T + \boldsymbol{\tau}^1(\boldsymbol{\tau}^1)^T + \boldsymbol{\tau}^2(\boldsymbol{\tau}^2)^T = \boldsymbol{I}. \tag{8}$$

We observe that, during the daytime, the difference $\psi_\varsigma - \psi_\chi$ is usually positive, resulting in a water flow from soil to root [15]. Additional comments on the choice of the interface condition (7) follow in Remark 1.

Summarizing, the 3D-3D problem for modeling the water exchange between soil and root reads as

$$\boldsymbol{u}_\varsigma = -K(\psi_\varsigma)\nabla[\psi_\varsigma + z] \qquad \text{in } D^j, \tag{9}$$

$$C(\psi_\varsigma)\frac{\partial\psi_\varsigma}{\partial t} + \mathrm{div}\boldsymbol{u}_\varsigma = 0 \qquad \text{in } D^j, \tag{10}$$

$$\psi_\varsigma = 0 \qquad \text{on } \partial D, \tag{11}$$

$$\boldsymbol{u}_\varsigma \cdot \boldsymbol{n}_\varsigma = \mu(\psi_\varsigma - \psi_\chi) \qquad \text{on } \Gamma^j, \tag{12}$$

$$-\mathrm{div}\boldsymbol{\sigma}_\chi + K_a \boldsymbol{u}_\chi = -\rho g \boldsymbol{e}_z \qquad \text{in } \Sigma^j, \tag{13}$$

$$\mathrm{div}\boldsymbol{u}_\chi = 0 \qquad \text{in } \Sigma^j, \tag{14}$$

$$\boldsymbol{\sigma}_\chi \boldsymbol{n}_\chi = \boldsymbol{0} \qquad \text{on } \partial\Sigma_{\text{collar}} \cup \partial\Sigma^j_{\text{tip}}, \tag{15}$$

$$\boldsymbol{u}_\chi \cdot \boldsymbol{n}_\chi = \mu(\psi_\chi - \psi_\varsigma) \qquad \text{on } \Gamma^j, \tag{16}$$

$$\boldsymbol{u}_\chi \cdot \boldsymbol{\tau}^d = 0, \ d = 1,2 \qquad \text{on } \Gamma^j, \tag{17}$$

equipped with initial conditions for the soil pressure head ψ_ς on the initial geometry D^0.

3. The model reduction and the PDE-constrained optimization problem

To reduce the computational burden of simulations, root inclusions are often identified with their centerlines, hence avoiding the definition of a 3D mesh in such thin and elongated domains, and leading to a so-called *3D-1D coupled problem*.

Since a bounded trace operator is not defined in standard Sobolev spaces between manifolds having codimension bigger than one, deriving a well-posed formulation for 3D-1D coupled problems is non-trivial and the research on the subject is still active. Different

approaches have been investigated in literature to tackle this issue, including the introduction of suitable weighted Sobolev spaces [34,35], and the use of regularization [36–38] or splitting [39,40] techniques to treat the singular terms. In [41] proper averaging operators were introduced to perform a geometrical model reduction from a 3D-3D to a 3D-1D problem and in [42] the coupling was tackled by means of Lagrange multipliers in a domain-decomposition setting.

Here, we follow the approach proposed in [43], by assuming that the quantities of interest have a negligible variation on the cross-sections of the inclusions, and introducing proper subspaces of Sobolev spaces to reflect the main model assumptions.

Thus, to perform the geometric model reduction leading to the 3D-1D problem, we now make some fundamental assumptions. Let us consider a cylindrical coordinate system around the axis of Σ^j, for all $j = 0, \dots, J$. We denote by $\boldsymbol{e}_r$, $\boldsymbol{e}_\beta$, and $\boldsymbol{e}_s$ the radial, the angular and the axial unit vectors, respectively, whereas (r, β, s) are the related coordinates with $r \in [0, R)$, $\beta \in [0, 2\pi)$, $s \in [0, S^j]$. Let us then assume that (see also [44,45]):

A.1 The root segment is rigid and rectilinear. Thus, we neglect the effect of pressure on root volume.

A.2 Each cross-section is assumed to be circular with a constant radius R. In particular, R does not depend on the axial coordinates s.

A.3 We assume that all quantities are independent of the angular coordinate β and, in particular, that the xylem pressure head ψ_χ is constant on each section, that is at each time $t \in \mathcal{I}_j$, $j = 1, \dots, J$,

$$\psi_\chi(t, r, \beta, s) = \hat{\psi}_\chi(t, s), \quad \forall r \in [0, R),\ \beta \in [0, 2\pi),\ s \in [0, S^j],$$

where $\hat{\psi}_\chi$ varies only with time and along the axial coordinate s.

A.4 The rotational velocity is negligible with respect to the axial velocity, i.e., in cylindrical coordinates, at each time $t \in \mathcal{I}_j$, $\forall j = 1, \dots, J$, we can write

$$\boldsymbol{u}_\chi = \begin{bmatrix} (\boldsymbol{u}_\chi)_r \\ (\boldsymbol{u}_\chi)_\beta \\ (\boldsymbol{u}_\chi)_s \end{bmatrix} = \begin{bmatrix} 0 \\ 0 \\ (\boldsymbol{u}_\chi)_s \end{bmatrix}, \quad \forall r \in [0, R),\ \beta \in [0, 2\pi),\ s \in [0, S^j]. \tag{18}$$

We further assume that the axial component of the xylem velocity can be defined as $(\boldsymbol{u}_\chi)_s(t, r, \beta, s) = \hat{u}_\chi(t, s) f(rR^{-1})$, where $\hat{u}_\chi$ is the mean axial velocity on the cross-section $\Sigma^j(s)$ at the time t, i.e.

$$\hat{u}_\chi(t, s) = \frac{1}{|\Sigma^j(s)|} \int_{\Sigma^j(s)} (\boldsymbol{u}_\chi)_s \quad \forall s \in [0, S^j],$$

and $f : [0, 1] \to \mathbb{R}$, $f \in C^\infty([0, 1])$ is a radial velocity profile which satisfies

$$\int_0^1 f(y) y \, dy = \frac{1}{2}. \tag{19}$$

An example of such function f, which can be found in [44], is given by

$$f(y) = \frac{\gamma + 2}{\gamma}(1 - y^\gamma) \quad \text{for some } \gamma \in \mathbb{R}. \tag{20}$$

We observe that, for $\gamma = 2$, the function (20) reduces to the well-known Hagen-Poiseuille solution in a pipe of uniform (circular) cross-section.

Under Assumption A.4, at each time $t \in \mathcal{I}_j$, Eq. (14), i.e., the mass conservation equation for the xylem, reduces to

$$\frac{\partial (\boldsymbol{u}_\chi)_s}{\partial s} = 0 \quad \text{in } \Sigma^j. \tag{21}$$

Let us define, as in [43,46], the following two uniform extension operators

$$\mathcal{E}_\Sigma : H^1(\Lambda^j) \to H^1(\Sigma^j) \text{ and } \mathcal{E}_\Gamma : H^1(\Lambda^j) \to H^{1/2}(\Gamma^j)$$

defined such that, given $\hat{q} \in H^1(\Lambda^j)$, $\forall s \in [0, S^j]$, $\mathcal{E}_\Sigma \hat{q}$ is the uniform extension of the pointwise value $\hat{q}(s)$ to the cross-section $\Sigma^j(s)$ and $\mathcal{E}_\Gamma \hat{q}$ is the uniform extension of $\hat{q}(s)$ to the boundary $\Gamma^j(s)$ of the same cross-section, i.e.

$$\left(\mathcal{E}_\Sigma \hat{q}\right)(\boldsymbol{x}) = \hat{q}(s)\ \forall \boldsymbol{x} \in \Sigma^j(s) \quad \text{and} \quad \left(\mathcal{E}_\Gamma \hat{q}\right)(\boldsymbol{x}) = \hat{q}(s)\ \forall \boldsymbol{x} \in \Gamma^j(s).$$

Finally, we consider the trace operator

$$\gamma_\Gamma : H^1(\Sigma^j) \to H^{1/2}(\Gamma^j) \text{ such that } \gamma_\Gamma q = q_{|\Gamma^j}\ \forall q \in H^1(\Sigma^j).$$

Now, we can introduce the following spaces

$$\hat{\mathcal{V}}_\chi = H^1(\Lambda^j), \quad \hat{\mathcal{Q}}_\chi = H^1_0(\Lambda^j),$$

$$\mathcal{V}_\chi = \left\{ \boldsymbol{v}_\chi = \begin{bmatrix} 0 \\ 0 \\ (\boldsymbol{v}_\chi)_s \end{bmatrix} \in [H^1(\Sigma^j)]^3 : (\boldsymbol{v}_\chi)_s = \hat{v}_\chi f(rR^{-1}) \text{ with } \hat{v}_\chi \in \hat{\mathcal{V}}_\chi \right\},$$

$$\mathcal{Q}_\chi = \{ q_\chi \in H^1(\Sigma^j) : q_\chi = \mathcal{E}_\Sigma \hat{q}_\chi,\ \hat{q}_\chi \in \hat{\mathcal{Q}}_\chi \},$$

and write the variational formulation of the root problem as: *Find* $\boldsymbol{u}_\chi \in \mathcal{V}_\chi$, $\psi_\chi \in \mathcal{Q}_\chi$ *such that*

$$\left(\nu\nabla\boldsymbol{u}_\chi, \nabla\boldsymbol{v}_\chi\right)_{\Sigma^j} + \left(k_a\boldsymbol{u}_\chi, \boldsymbol{v}_\chi\right)_{\Sigma^j} - \left(\psi_\chi, \mathrm{div}\boldsymbol{v}_\chi\right)_{\Sigma^j} = -\left(\boldsymbol{e}_z, \boldsymbol{v}_\chi\right)_{\Sigma^j} \qquad \forall \boldsymbol{v}_\chi \in \mathcal{V}_\chi, \tag{22}$$

$$\left(\mathrm{div}\boldsymbol{u}_\chi, q_\chi\right)_{\Sigma^j} = 0 \qquad \forall q_\chi \in \mathcal{Q}_\chi, \tag{23}$$

where we denote by $\nu = \frac{\bar{\nu}}{\rho g}$ and $k_a = \frac{K_a}{\rho g}$.

Thanks to the above regularity assumptions, problem (22)-(23) can be easily reduced to a 1D problem following an approach similar to the one presented in [43]. Let us start by considering Eq. (23): integration by parts and the interface condition (16) yield

$$\begin{aligned} 0 &= \left(\mathrm{div}\boldsymbol{u}_\chi, q_\chi\right)_{\Sigma^j} = -\left(\boldsymbol{u}_\chi, \nabla q_\chi\right)_{\Sigma^j} + \left(\boldsymbol{u}_\chi\cdot\boldsymbol{n}_\chi, q_\chi\right)_{\partial\Sigma^j} \\ &= -\left(\boldsymbol{u}_\chi, \nabla q_\chi\right)_{\Sigma^j} + \left(\boldsymbol{u}_\chi\cdot\boldsymbol{n}_\chi, q_\chi\right)_{\partial\Sigma^j_{\mathrm{tip}}} + \left(\boldsymbol{u}_\chi\cdot\boldsymbol{n}_\chi, q_\chi\right)_{\partial\Sigma_{\mathrm{collar}}} + \left(\mu(\gamma_\Gamma\psi_\chi - \gamma_\Gamma\psi_\varsigma), \gamma_\Gamma q_\chi\right)_{\Gamma^j} \end{aligned} \tag{24}$$

Let us first of all observe that, according to Assumption A.4, $\forall q_\chi \in \mathcal{Q}_\chi$ and $\hat{q}_\chi \in \hat{\mathcal{Q}}_\chi : \gamma_\Gamma q_\chi = \mathcal{E}_\Sigma \hat{q}_\chi$

$$\begin{aligned} \left(\boldsymbol{u}_\chi, \nabla q_\chi\right)_{\Sigma^j} &= \int_0^{S^j}\int_0^{2\pi}\int_0^R \hat{u}_\chi f(rR^{-1})\frac{\partial\hat{q}_\chi}{\partial s} r\, dr\, d\beta\, ds \\ &= 2\pi R^2\Big(\int_0^1 f(y)y\, dy\Big)\Big(\int_0^{S^j}\hat{u}_\chi\frac{\partial\hat{q}_\chi}{\partial s}ds\Big) = \left(\pi R^2\hat{u}_\chi, \frac{\partial\hat{q}_\chi}{\partial s}\right)_{\Lambda^j}. \end{aligned} \tag{25}$$

Similarly, denoting by $\Sigma^j(\bar{s})$ a generic transversal section obtained by cutting Σ^j at $\bar{s} \in [0, S_j]$ with a plane orthogonal to Λ^j we have

$$\left(\boldsymbol{u}_\chi\cdot\boldsymbol{e}_s, q_\chi\right)_{\Sigma^j(\bar{s})} = \pi R^2\hat{u}_\chi(\bar{s})\,\hat{q}_\chi(\bar{s}), \quad \forall q_\chi \in \mathcal{Q}_\chi,\ \hat{q}_\chi \in \hat{\mathcal{Q}}_\chi : \gamma_\Gamma q_\chi = \mathcal{E}_\Sigma\hat{q}_\chi. \tag{26}$$

Furthermore, according to Assumption A.3,

$$\left(\gamma_\Gamma\psi_\chi, \gamma_\Gamma q_\chi\right)_{\Gamma^j} = \left(2\pi R\hat{\psi}_\chi, \hat{q}_\chi\right)_{\Lambda^j}, \quad \forall q_\chi \in \mathcal{Q}_\chi,\ \hat{q}_\chi \in \hat{\mathcal{Q}}_\chi : \gamma_\Gamma q_\chi = \mathcal{E}_\Sigma\hat{q}_\chi. \tag{27}$$

Finally, introducing the spaces

$$\mathcal{H}_\Gamma = \{\phi \in H^{1/2}(\Gamma^j) :\ \phi = \mathcal{E}_\Gamma\hat{\phi},\ \hat{\phi} \in \hat{\mathcal{Q}}_\chi\},$$

$$\mathcal{Q}_\varsigma = \{q_\varsigma \in H^1(D) :\ \gamma_\Gamma q_\varsigma \in \mathcal{H}_\Gamma \text{ and } q_\varsigma = 0 \text{ on } \partial D\}$$

and assuming that $\psi_\varsigma \in \mathcal{Q}_\varsigma$, we similarly obtain

$$\left(\gamma_\Gamma\psi_\varsigma, \gamma_\Gamma q_\chi\right)_{\Gamma^j} = \left(2\pi R\hat{\psi}_\varsigma, \hat{q}_\chi\right)_{\Lambda^j}, \quad \forall q_\chi \in \mathcal{Q}_\chi,\ \hat{q}_\chi \in \hat{\mathcal{Q}}_\chi : \gamma_\Gamma q_\chi = \mathcal{E}_\Sigma\hat{q}_\chi \tag{28}$$

where $\hat{\psi}_\varsigma \in \hat{\mathcal{Q}}_\chi :\ \mathcal{E}_\Gamma\hat{\psi}_\varsigma = \gamma_\Gamma\psi_\varsigma$. Going now back to (24) and exploiting (25)-(28), along with the fundamental theorem of calculus, we obtain

$$\begin{aligned} 0 &= -\left(\pi R^2\hat{u}_\chi, \frac{\partial\hat{q}_\chi}{\partial s}\right)_{\Lambda^j} + \pi R^2\hat{u}_\chi(S^j)\,\hat{q}_\chi(S^j) - \pi R^2\hat{u}_\chi(0)\,\hat{q}_\chi(0) + \left(\mu(\hat{\psi}_\chi - \hat{\psi}_\varsigma), \hat{q}_\chi\right)_{\Lambda^j} \\ &= -\int_0^{S^j}\pi R^2\hat{u}_\chi\frac{\partial\hat{q}_\chi}{\partial s}ds + \int_0^{S^j}\pi R^2\frac{\partial(\hat{u}_\chi\,\hat{q}_\chi)}{\partial s}ds + \int_0^{S^j}2\pi R\mu(\hat{\psi}_\chi - \hat{\psi}_\varsigma)\hat{q}_\chi ds \\ &= \left(\pi R^2\frac{\partial\hat{u}_\chi}{\partial s}, \hat{q}_\chi\right)_{\Lambda^j} + \left(2\pi R\mu(\hat{\psi}_\chi - \hat{\psi}_\varsigma), \hat{q}_\chi\right)_{\Lambda^j}, \quad \forall q_\chi \in \mathcal{Q}_\chi,\ \hat{q}_\chi \in \hat{\mathcal{Q}}_\chi : \gamma_\Gamma q_\chi = \mathcal{E}_\Sigma\hat{q}_\chi. \end{aligned}$$

Concerning Eq. (22), we have that

$$\left(\psi_\chi, \mathrm{div}\boldsymbol{v}_\chi\right)_{\Sigma^j} = \int_{\Lambda^j}\pi R^2\frac{\partial\hat{v}_\chi}{\partial s}\hat{\psi}_\chi, \quad \left(\boldsymbol{e}_z, \boldsymbol{v}_\chi\right)_{\Sigma^j} = \int_{\Lambda^j}\pi R^2\boldsymbol{e}_z\cdot\boldsymbol{e}_s\hat{v}_\chi.$$

Moreover, due to (21) and the fact that, for any $\boldsymbol{v}_\chi \in \mathcal{V}_\chi$

$$\frac{\partial(\boldsymbol{v}_\chi)_s}{\partial r} = R^{-1}f'(rR^{-1})\hat{v}_\chi,$$

we obtain

$$\nabla\boldsymbol{u}_\chi = \begin{bmatrix} 0 & 0 & 0 \\ 0 & 0 & 0 \\ R^{-1}f'(rR^{-1})\hat{u}_\chi & 0 & 0 \end{bmatrix}, \quad \nabla\boldsymbol{v}_\chi = \begin{bmatrix} 0 & 0 & 0 \\ 0 & 0 & 0 \\ R^{-1}f'(rR^{-1})\hat{v}_\chi & 0 & \frac{\partial(\boldsymbol{v}_\chi)_s}{\partial s} \end{bmatrix}, \tag{29}$$

and hence

$$\left(\nu\nabla\boldsymbol{u}_\chi, \nabla\boldsymbol{v}_\chi\right)_{\Sigma^j} + \left(k_a\boldsymbol{u}_\chi, \boldsymbol{v}_\chi\right)_{\Sigma^j} = \int_{\Lambda^j}\nu\hat{u}_\chi\hat{v}_\chi F' + \int_{\Lambda^j}k_a\hat{u}_\chi\hat{v}_\chi F = \left(k_\chi\hat{u}_\chi, \hat{v}_\chi\right)_{\Lambda^j},$$

with $F, F' \in \mathbb{R}$ defined as

$$F := 2\pi R^2 \int_0^1 [f(y)]^2 y \, dy, \quad F' := 2\pi \int_0^1 [f'(y)]^2 y \, dy,$$

and $k_\chi = F k_a + F' \nu$.

Remark 1. For the sake of simplicity, in (7) (and hence (17)) we imposed no-slip conditions for the tangential velocity. Nevertheless, more complex conditions could also be considered. For instance, the Beavers-Joseph-Saffman condition (see [47]) is commonly used to describe the interface between free-fluid and porous regions, as well as the interface in dual-porosity media:

$$-\boldsymbol{n}_\chi \cdot (\boldsymbol{\sigma}_\chi \boldsymbol{\tau}^d) = \alpha_d \boldsymbol{u}_\chi \cdot \boldsymbol{\tau}^d, \quad \forall d = 1, 2 \quad \text{on } \Gamma.$$

We observe that imposing such an interface condition only leads to a redefinition of the coefficient k_χ in the reduced problem. Moreover, we note that the proposed shape (20) for the radial profile f is consistent with the no-slip conditions applied to the xylem velocity. Nonetheless, alternative forms for f can also be adopted to accommodate the Beavers-Joseph-Saffman condition. Indeed, the only requirement for f is that it must satisfy the property (19).

Concerning the equations for the soil volume, we proceed as in [43] by rewriting the soil problem in the primal form. We hence look for $\psi_\varsigma \in \mathcal{Q}_\varsigma$ such that

$$\left(C(\psi_\varsigma)\frac{\partial \psi_\varsigma}{\partial t}, q_\varsigma\right)_{\mathcal{D}^j} + \left(K(\psi_\varsigma)\nabla\psi_\varsigma, \nabla q_\varsigma\right)_{\mathcal{D}^j} + \left(\mu(\gamma_\Gamma\psi_\varsigma - \gamma_\Gamma\psi_\chi), \gamma_\Gamma q_\varsigma\right)_\Gamma + \left(K(\psi_\varsigma)\boldsymbol{e}_z, \nabla q_\varsigma\right)_{\mathcal{D}^j} = 0 \quad \forall q_\varsigma \in \mathcal{Q}_\varsigma.$$

As for the mass balance equation, the integral over the lateral surface Γ^j can be reduced to an integral over the centerline Λ^j as

$$\left(\mu(\gamma_\Gamma\psi_\varsigma - \gamma_\Gamma\psi_\chi), \gamma_\Gamma q_\varsigma\right)_\Gamma = \left(2\pi R\mu(\widehat{\psi}_\varsigma - \widehat{\psi}_\chi), \widehat{q}_\varsigma\right)_{\Lambda^j}.$$

Finally, we obtain the following 3D-1D coupled problem: *At each time $t \in \mathcal{I}_j$, for $j = 1, \dots, J$, find $(\psi_\varsigma, \widehat{u}_\chi, \widehat{\psi}_\chi) \in \mathcal{Q}_\varsigma \times \widehat{\mathcal{V}}_\chi \times \widehat{\mathcal{Q}}_\chi$ such that*

$$\begin{cases} \left(C(\psi_\varsigma)\frac{\partial\psi_\varsigma}{\partial t}, q_\varsigma\right)_{\mathcal{D}^j} + \left(K(\psi_\varsigma)\nabla\psi_\varsigma, \nabla q_\varsigma\right)_{\mathcal{D}^j} + \left(2\pi R\mu(\widehat{\psi}_\varsigma - \widehat{\psi}_\chi), \widehat{q}_\varsigma\right)_{\Lambda^j} + \left(K(\psi_\varsigma)\boldsymbol{e}_z, \nabla q_\varsigma\right)_{\mathcal{D}^j} = 0 & \forall q_\varsigma \in \mathcal{Q}_\varsigma, \\ \left(k_\chi \widehat{u}_\chi, \widehat{v}_\chi\right)_{\Lambda^j} - \left(\widehat{\psi}_\chi, \pi R^2 \frac{\partial \widehat{v}_\chi}{\partial s}\right)_{\Lambda^j} = -\left(\pi R^2 \boldsymbol{e}_z \cdot \boldsymbol{e}_s, \widehat{v}_\chi\right)_{\Lambda^j} & \forall \widehat{v}_\chi \in \widehat{\mathcal{V}}_\chi, \\ \left(\pi R^2 \frac{\partial \widehat{u}_\chi}{\partial s}, \widehat{q}_\chi\right)_{\Lambda^j} + \left(2\pi R\mu(\widehat{\psi}_\chi - \widehat{\psi}_\varsigma), \widehat{q}_\chi\right)_{\Lambda^j} = 0 & \forall \widehat{q}_\chi \in \widehat{\mathcal{Q}}_\chi. \end{cases} \tag{30}$$

We highlight that the reduction procedure results in a Darcy-like problem in mixed form for the xylem sap.

3.1. PDE-constrained optimization problem

Instead of solving the set of coupled equations summarized in Problem (30), we here recast the problem into a PDE-constrained optimization problem. First of all, adopting a domain decomposition approach, we introduce two auxiliary variables $\phi_\varsigma, \phi_\chi \in \mathcal{H}_\Gamma$ such that

$$\left(\gamma_\Gamma\psi_\varsigma - \phi_\varsigma, \eta\right)_{\mathcal{H}_\Gamma} = 0 \qquad \forall \eta \in \mathcal{H}_\Gamma, \tag{31}$$

$$\left(\gamma_\Gamma\psi_\chi - \phi_\chi, \eta\right)_{\mathcal{H}_\Gamma} = 0 \qquad \forall \eta \in \mathcal{H}_\Gamma. \tag{32}$$

Denoting by $\widehat{\phi}_\varsigma, \widehat{\phi}_\chi \in \widehat{\mathcal{Q}}_\chi$ the one dimensional variables such that $\mathcal{E}_\Gamma\widehat{\phi}_\varsigma = \gamma_\Gamma\phi_\varsigma$ and $\mathcal{E}_\Gamma\widehat{\phi}_\chi = \gamma_\Gamma\phi_\chi$, Problem (30) can be rewritten as: *at each time $t \in \mathcal{I}_j$, for $j = 1, \dots, J$, find $(\psi_\varsigma, \widehat{u}_\chi, \widehat{\psi}_\chi, \widehat{\phi}_\varsigma, \widehat{\phi}_\chi) \in \mathcal{Q}_\varsigma \times \widehat{\mathcal{V}}_\chi \times \widehat{\mathcal{Q}}_\chi \times \widehat{\mathcal{Q}}_\chi \times \widehat{\mathcal{Q}}_\chi$ such that*

$$\left(C(\psi_\varsigma)\frac{\partial\psi_\varsigma}{\partial t}, q_\varsigma\right)_{\mathcal{D}^j} + \left(K(\psi_\varsigma)\nabla\psi_\varsigma, \nabla q_\varsigma\right)_{\mathcal{D}^j} + \left(2\pi R\mu(\widehat{\psi}_\varsigma - \widehat{\phi}_\chi), \widehat{q}_\varsigma\right)_{\Lambda^j} + \left(K(\psi_\varsigma)\boldsymbol{e}_z, \nabla q_\varsigma\right)_{\mathcal{D}^j} = 0 \qquad \forall q_\varsigma \in \mathcal{Q}_\varsigma, \tag{33}$$

$$\left(k_\chi \widehat{u}_\chi, \widehat{v}_\chi\right)_{\Lambda^j} - \left(\widehat{\psi}_\chi, \pi R^2 \frac{\partial \widehat{v}_\chi}{\partial s}\right)_{\Lambda^j} = -\left(\pi R^2 \boldsymbol{e}_z \cdot \boldsymbol{e}_s, \widehat{v}_\chi\right)_{\Lambda^j} \qquad \forall \widehat{v}_\chi \in \widehat{\mathcal{V}}_\chi, \tag{34}$$

$$\left(\pi R^2 \frac{\partial \widehat{u}_\chi}{\partial s}, \widehat{q}_\chi\right)_{\Lambda^j} + \left(2\pi R\mu(\widehat{\psi}_\chi - \widehat{\phi}_\varsigma), \widehat{q}_\chi\right)_{\Lambda^j} = 0 \qquad \forall \widehat{q}_\chi \in \widehat{\mathcal{Q}}_\chi, \tag{35}$$

$$\left(\gamma_\Gamma\psi_\varsigma - \mathcal{E}_\Gamma\widehat{\phi}_\varsigma, \mathcal{E}_\Gamma\widehat{\eta}\right)_{\mathcal{H}_\Gamma} = 0 \qquad \forall \widehat{\eta} \in \widehat{\mathcal{Q}}_\chi, \tag{36}$$

$$\left(\mathcal{E}_\Gamma\widehat{\psi}_\chi - \mathcal{E}_\Gamma\widehat{\phi}_\chi, \mathcal{E}_\Gamma\widehat{\eta}\right)_{\mathcal{H}_\Gamma} = 0 \qquad \forall \widehat{\eta} \in \widehat{\mathcal{Q}}_\chi. \tag{37}$$

Conditions (36)-(37), i.e. (31)-(32), are replaced by the minimization of a cost functional, measuring the error committed in the fulfillment of such constraints. Let

$$\mathcal{J}(\widehat{\phi}_\varsigma, \widehat{\phi}_\chi) = \frac{1}{2}\left(\|\gamma_\Gamma \psi_\varsigma(\widehat{\phi}_\chi) - \mathcal{E}_\Gamma \widehat{\phi}_\varsigma\|^2_{\mathcal{H}_\Gamma} + \|\mathcal{E}_\Gamma \widehat{\psi}_\chi(\widehat{\phi}_\varsigma) - \mathcal{E}_\Gamma \widehat{\phi}_\chi\|^2_{\mathcal{H}_\Gamma} \right). \tag{38}$$

The final optimal control problem reads:

$$\begin{aligned} &\textit{At each time } t \in \mathcal{I}_j, \textit{ for } j = 1, \dots, J, \\ &\textit{find } (\psi_\varsigma, \hat{u}_\chi, \hat{\psi}_\chi, \widehat{\phi}_\varsigma, \widehat{\phi}_\chi) \in \mathcal{Q}_\varsigma \times \widehat{\mathcal{V}}_\chi \times \widehat{\mathcal{Q}}_\chi \times \widehat{\mathcal{Q}}_\chi \times \widehat{\mathcal{Q}}_\chi \textit{ such that} \\ &\quad \textit{the functional (38) is minimized subject to (33)–(35).} \end{aligned} \tag{39}$$

There are several advantages of solving the problem in a PDE-constrained optimization framework. First, there is great flexibility in the choice of the meshes: no mesh conformity is required between the 3D soil and the 1D roots and the different one-dimensional variables can be meshed independently. Second, the introduction of the auxiliary variables allows the direct computation of interface variables without any need of post-processing. This can be interesting, for example, to easily monitor the flux exchanged at the interface as the root network grows. Let us remark that, in the case of a single or just a few root segments, the size of the saddle-point system (33)–(37) is mainly determined by the 3D variables, and adopting an optimization-based approach may offer limited benefit, while increasing the number of degrees of freedom. However, when an extended RSA is considered, the number of 3D and 1D degrees of freedom can become comparable. In this scenario, the optimization-based approach becomes significantly more beneficial. Indeed, as we will clarify in Section 4.4, it avoids the resolution of a big saddle-point system and it enables instead the decoupling of the 3D and 1D sub-problems, which can be solved independently at each iteration of the conjugate gradient scheme. The key feature of the optimization-based approach is hence related to its scalability, as it facilitates parallelization and allows the method to efficiently handle large systems. Furthermore, when the size of the 3D problem becomes too large, parallelization of the 3D system using standard domain decomposition techniques is feasible and can be fully integrated into our approach.

3.2. Managing the intersections between root segments

Accounting for the growth of the RSA and the creation of root branches raises the question on how a more complex Σ^j, characterized by the presence of multiple intersecting root segments, can be tackled.

For each time interval $\mathcal{I}_j$, we assume that Σ^j can be covered by a set of straight cylindrical root segments $\{\Sigma^j_i\}_{i\in\mathcal{Y}^j}$, with $\mathcal{Y}^j$ being the set of indexes of root segments at time t_j. We denote by Γ^j_i the lateral surface of Σ^j_i, and by $\Lambda^j_i = \{\lambda(s),\ s \in (0_i, S_i)\}$ its centerline. We assume that there is no overlap among the centerlines of different root segments and that their closure can intersect at most in one point $\boldsymbol{x}_b = \lambda(s_b)$, $b \in \mathcal{B}^j$. Furthermore, let

$$\Lambda^j = \Big(\bigcup_{i\in\mathcal{Y}^j} \Lambda^j_i\Big) \cup \{\boldsymbol{x}_b\}_{b\in\mathcal{B}^j}.$$

We denote by $\mathcal{Y}^j_b$ the set of indexes of the segments that are adjacent to an intersection point $\boldsymbol{x}_b$ and by $\#\mathcal{Y}^j_b$ its cardinality. We use $\Lambda^{j,+}_i = \lambda(s^+_b)$ and $\Lambda^{j,-}_i = \lambda(s^-_b)$ to denote the inflow and outflow end-point of Λ^j_i, respectively. Clearly s^+_b and s^-_b can be either 0_i or S_i for each $i \in \mathcal{Y}^j$. Similarly, we split $\mathcal{Y}^j_b$ as $\mathcal{Y}^j_b = \mathcal{Y}^{j,+}_b \cup \mathcal{Y}^{j,-}_b$ to distinguish between the segments through which the flux enters in $\boldsymbol{x}_b$, indexed by $i \in \mathcal{Y}^{j,+}_b$ and the ones through which it exits, indexed by $i \in \mathcal{Y}^{j,-}_b$.

The model reduction proposed in Section 3 can be performed separately for each root segment, provided that proper conditions are imposed. As in [46], we introduce, for each $\boldsymbol{x}_b$, an *extended intersection volume* $\mathcal{V}_b$ (see Fig. 2), whose diameter is assumed to be much smaller than the minimum length of the intersecting root segments. In particular, we assume that

A.5 in the intersection volume, the xylem pressure p_χ has a unique constant value, coinciding with the value in $\boldsymbol{x}_b$ and denoted by p^b_χ.

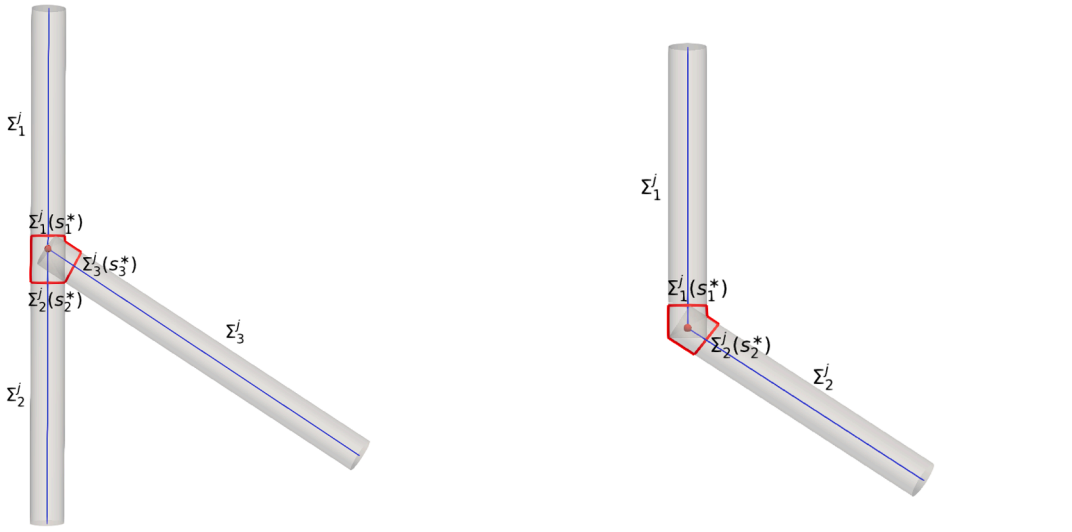
The two configurations reported in Fig. 2 refer to the most common cases of root segment intersection which can occur in the proposed growth model: in Fig. 2a branch originates from a straight root segment, which is in turn split at the branching point into two root segments; in Fig. 2b a change in the growth direction produces two adjacent segments with different orientation, which are treated as two intersecting straight segments. In both cases, the faces $\Sigma^j_i(s^*_i)$, $i \in \mathcal{Y}^j_b$ (see Fig. 2), which belong to the boundary of the intersection volume, can be seen as the extreme sections of disjoint sub-cylinders on which the trace operator γ_Γ and extension operators $\mathcal{E}_\Sigma$, $\mathcal{E}_\Gamma$ are well defined. By an abuse of notation, we will still denote such sub-cylinders as Σ^j_i.

Denoting by $\boldsymbol{v}_{\chi,i}$ and by $\psi_{\chi,i}$ the restrictions of functions in $\boldsymbol{\mathcal{V}}_\chi$ and in $\mathcal{Q}_\chi$ to Σ^j_i for each $i \in \mathcal{Y}^j$, respectively, Eqs. (22)-(23) can be written as

$$\begin{aligned} &\sum_{i\in\mathcal{Y}^j} \left[\left(\nu\nabla\boldsymbol{u}_{\chi,i}, \nabla\boldsymbol{v}_{\chi,i}\right)_{\Sigma^j_i} + \left(k_a\boldsymbol{u}_{\chi,i}, \boldsymbol{v}_{\chi,i}\right)_{\Sigma^j_i} - \left(\psi_{\chi,i}, \mathrm{div}\boldsymbol{v}_{\chi,i}\right)_{\Sigma^j_i} + \left(\boldsymbol{e}_z, \boldsymbol{v}_{\chi,i}\right)_{\Sigma^j_i} \right] - \sum_{b\in\mathcal{B}^j} \sum_{i\in\mathcal{Y}^j_b} \left(\frac{\boldsymbol{n}^T_{\chi,i}(\boldsymbol{\sigma}_{\chi,i}\boldsymbol{n}_{\chi,i})}{\rho g}, \boldsymbol{v}_{\chi,i}\cdot\boldsymbol{n}_{\chi,i} \right)_{\Sigma^j_i(s^*_i)} \\ &\qquad = 0 \forall \boldsymbol{v}_\chi \in \boldsymbol{\mathcal{V}}_\chi, \sum_{i\in\mathcal{Y}^j} \left(\mathrm{div}\boldsymbol{u}_{\chi,i}, q_{\chi,i}\right)_{\Sigma^j_i} = 0 \forall q_\chi \in \mathcal{Q}_\chi. \end{aligned}$$

These equations must be coupled with proper matching conditions at the interfaces with the extended intersection volume. To impose flux conservation at the intersection points, we impose flux conservation inside the intersection volumes, i.e.

$$\sum_{i\in\mathcal{Y}^j_b} (\boldsymbol{u}_{\chi,i}\cdot\boldsymbol{n}_{\chi,i})_{|\Sigma^j_i(s^*_i)} = 0 \quad \forall b \in \mathcal{B}^j. \tag{40}$$



(a) Branch originating from a parent root segment. (b) Adjacent root segments with different orientation.

Fig. 2. Nomenclature at branching points. The boundaries of the extended intersection volume are highlighted in red.

Let us remark that $\boldsymbol{n}_{\chi,i} = \boldsymbol{e}_s$ on $\Sigma_i^j(s_i^*)$ and that, according to Assumption A.4,

$$\boldsymbol{u}_{\chi,i} \cdot \boldsymbol{e}_s = f(rR^{-1})\widehat{u}_{\chi,i}.$$

Condition (40) can hence be rewritten as

$$\sum_{i\in\mathcal{Y}_b^{j,+}} (\widehat{u}_{\chi,i})_{|\Lambda_i^{j,-}} - \sum_{i\in\mathcal{Y}_b^{j,-}} (\widehat{u}_{\chi,i})_{|\Lambda_i^{j,+}} = 0, \quad \forall b \in \mathcal{B}^j,$$

and, since it is essential for the flux, we can impose it directly into the function space, redefining $\widehat{\mathcal{V}}_\chi$ as

$$\widehat{\mathcal{V}}_\chi = \left\{ \widehat{v}_\chi \in \bigcup_{i\in\mathcal{Y}^j} H^1(\Lambda_i^j) : \left[\sum_{i\in\mathcal{Y}_b^{j,+}} (\widehat{v}_{\chi,i})_{|\Lambda_i^{j,-}} - \sum_{i\in\mathcal{Y}_b^{j,-}} (\widehat{v}_{\chi,i})_{|\Lambda_i^{j,+}} \right] = 0, \quad \forall b \in \mathcal{B}^j \right\}. \tag{41}$$

Recalling that $\boldsymbol{\sigma}_\chi = -p_\chi \boldsymbol{I} + \bar{\nu}\nabla\boldsymbol{u}_\chi$ and exploiting (29), the balance of normal forces at the interfaces with the intersection volume can hence be written as

$$(\boldsymbol{n}_{\chi,i}^T(\boldsymbol{\sigma}_{\chi,i}\boldsymbol{n}_{\chi,i}))_{|\Sigma_i^j(s_i^*)} = -p_\chi^b \quad \forall i \in \mathcal{Y}_b^j \quad \forall b \in \mathcal{B}^j. \tag{42}$$

Let us redefine $\widehat{\mathcal{Q}}_\chi$ as

$$\widehat{\mathcal{Q}}_\chi = \left\{ \widehat{q}_\chi \in C^0(\Lambda^j) : \widehat{q}_{\chi,i} \in H^1(\Lambda_i^j)\ \forall i \in \mathcal{Y}^j \text{ and } \widehat{q}_\chi = 0 \text{ at } \partial\Lambda_{\text{collar}} \cup \partial\Lambda_{\text{tip}}^j \right\}, \tag{43}$$

and let $\widehat{\psi}_\chi \in \widehat{\mathcal{Q}}_\chi$ be such that $\psi_{\chi|\Sigma_i^j} = (\mathcal{E}_\Sigma \widehat{\psi}_\chi)_{|\Sigma_i^j}$ and such that ψ_χ is the uniform extension to the whole intersection volume of $\widehat{\psi}_\chi^b = \frac{p_\chi^b}{\rho g}$. Then according to assumptions A.3–A.4 and exploiting (42) and the new definition of $\widehat{\mathcal{V}}_\chi$ we have that

$$-\sum_{i\in\mathcal{Y}_b^j} \left(\frac{\boldsymbol{n}_{\chi,i}^T(\boldsymbol{\sigma}_{\chi,i}\boldsymbol{n}_{\chi,i})}{\rho g}, \boldsymbol{v}_{\chi,i}\cdot\boldsymbol{n}_{\chi,i} \right)_{\Sigma_i^j(s_b)} = \pi R^2 \widehat{\psi}_\chi^b \left[\sum_{i\in\mathcal{Y}_b^{j,+}} (\widehat{v}_{\chi,i})_{|\Lambda_i^{j,-}} - \sum_{i\in\mathcal{Y}_b^{j,-}} (\widehat{v}_{\chi,i})_{|\Lambda_i^{j,+}} \right] = 0 \quad \forall b \in \mathcal{B}^j. \tag{44}$$

Hence, we can conclude that the optimal control problem in the case of multiple cylinders reads as problem (39) where the norms on Λ^j are now defined as broken norms drawn according to the partition $\{\Lambda_i^j\}_{i\in\mathcal{Y}^j}$ and the 1D functional spaces are defined as in (41)-(43).

4. The problem discretization and the solving strategy

In this section, we provide the details on the discretization of problem (39). Root growth in the time interval $\mathcal{I}_j = (t_{j-1}, t_j]$ is tackled by means of a *continuous-discrete hybrid tip-tracking approach*, resorting to the resolution of an ordinary differential equation (ODE) governing the evolution of the position of root tips. This ODE is solved by a forward Euler scheme, leading to the RSA

configuration at time t_j. We then consider the evolution of the quantities of interest in the interval $\mathcal{I}_j = (t_{j-1}, t_j]$ on the new fixed geometry, using a backward Euler scheme on a sub-partition of $\mathcal{I}_j$. The space discretization of the soil sample is instead tackled by the Virtual Element Method. Using a polytopal discretization enhances the method with great flexibility in handling geometrically complex samples, characterized by different layers or impervious obstacles, such as stones. Finally, the space discretization of the 1D variables is carried out by a mixed formulation with continuous pressure, which imposes flux conservation at junctions in a strong way.

4.1. Discrete root growth

Let us denote by $\mathcal{P}_{\text{tip}}^{j-1}$ the set of root tips at time t_{j-1}. Following a tip-tracking approach, we assume the position $\boldsymbol{x}_P$ of a root tip $P \in \mathcal{P}_{\text{tip}}^{j-1}$ to evolve according to the following ODE:

$$\frac{d\boldsymbol{x}_P}{dt} = \boldsymbol{w}_P^j(\psi_\varsigma(t_{j-1}, \boldsymbol{x}_P), \theta(t_{j-1}, \boldsymbol{x}_P); \mathcal{G}). \tag{45}$$

The combined effects of different plant tropisms is summarized in the growth vector $\boldsymbol{w}_P^j$ that depends on environmental conditions such as soil pressure head and water content, but also on the genetics of the plant species under study and on the type of soil, through the set of possibly stochastic parameters collected in $\mathcal{G}$ [48]. We refer to Section 5 for the actual definition of $\boldsymbol{w}_P^j$. Setting $\Delta\mathcal{I}_j = t_j - t_{j-1}$ and denoting by $\boldsymbol{x}_P^{j-1}$ the position of a given root tip at time t_{j-1}, we discretize Eq. (45) using a forward Euler scheme, i.e., we update the tip position as

$$\boldsymbol{x}_P^j = \boldsymbol{x}_P^{j-1} + \Delta\mathcal{I}_j \boldsymbol{w}_P^j. \tag{46}$$

Moreover, as the RSA grows, existing roots can branch. Hence, the growth model needs to track not only the position of existing tips, but also the activation of branching nodes and the related initial growth direction. Both are again governed by a set of stochastic parameters depending on the genetics of the species. Further details are provided in Appendix A.

Denoting by $\mathcal{P}_{\text{tip}}^{j-1}$ and $\mathcal{P}_{\text{branch}}^{j-1}$ respectively the sets of tips and branching nodes at time t_{j-1}, we have that $\mathcal{P}_{\text{tip}}^{j} = \mathcal{P}_{\text{tip}}^{j-1} \cup \mathcal{P}_{\text{branch}}^{j-1}$. When the position of all the root tips in $\mathcal{P}_{\text{tip}}^{j}$ has been computed, either according to (46) or as the emergence of a new branch from a branching point, the new tips are connected to the originating tip or branching point by a straight line Λ_P, and the 1D root network is updated as

$$\Lambda^j = \Lambda^{j-1} \cup \bigcup_{P \in \mathcal{P}_{\text{tip}}^j} \Lambda_P,$$

which represents the fixed RSA on which the quantities of interest will evolve for $t \in \mathcal{I}_j$.

4.2. Time discretization of the constraint equations

A backward Euler scheme is adopted for the time discretization of the constraint Eqs. (33)–(35) for $t \in \mathcal{I}_j$. We consider a uniform partition of the interval $\mathcal{I}_j$ with a step $\Delta t \le \Delta\mathcal{I}_j$ and $t_{j,n} = t_{j-1} + n\Delta t$, $n \ge 0$. We use the superscript n to refer to the value of a quantity of interest at time $t_{j,n}$. The set of the time-discrete constraints in the time interval $\mathcal{I}_j$ hence reads as: *For each* $n = 1, \dots, N$, *find* $(\psi_\varsigma^n, \widehat{u}_\chi^n, \widehat{\psi}_\chi^n, \widehat{\phi}_\varsigma^n, \widehat{\phi}_\chi^n) \in \mathcal{Q}_\varsigma \times \widehat{\mathcal{V}}_\chi \times \widehat{\mathcal{Q}}_\chi \times \widehat{\mathcal{Q}}_\chi \times \widehat{\mathcal{Q}}_\chi$ *such that*

$$\begin{cases} \left(C(\psi_\varsigma^n)\frac{\psi_\varsigma^n - \psi_\varsigma^{n-1}}{\Delta t}, q_\varsigma\right)_\Omega + \left(K(\psi_\varsigma^n)\nabla\psi_\varsigma^n, \nabla q_\varsigma\right)_\Omega + \left(2\pi R\mu(\widehat{\psi}_\varsigma^n - \widehat{\phi}_\chi^n), \widehat{q}_\varsigma\right)_{\Lambda^j} + \left(K(\psi_\varsigma^n)\boldsymbol{e}_z, \nabla q_\varsigma\right)_\Omega = 0 & \forall q_\varsigma \in \mathcal{Q}_\varsigma, \\ \left(k_\chi \widehat{u}_\chi^n, \widehat{v}_\chi\right)_{\Lambda^j} - \left(\widehat{\psi}_\chi^n, \pi R^2 \frac{\partial \widehat{v}_\chi}{\partial s}\right)_{\Lambda^j} = -\left(\pi R^2 \boldsymbol{e}_z \cdot \boldsymbol{e}_s, \widehat{v}_\chi\right)_{\Lambda^j} & \forall \widehat{v}_\chi \in \widehat{\mathcal{V}}_\chi, \\ \left(\pi R^2 \frac{\partial \widehat{u}_\chi^n}{\partial s}, \widehat{q}_\chi\right)_{\Lambda^j} + \left(2\pi R\mu(\widehat{\psi}_\chi^n - \widehat{\phi}_\varsigma^n), \widehat{q}_\chi\right)_{\Lambda^j} = 0 & \forall \widehat{q}_\chi \in \widehat{\mathcal{Q}}_\chi, \end{cases} \tag{47}$$

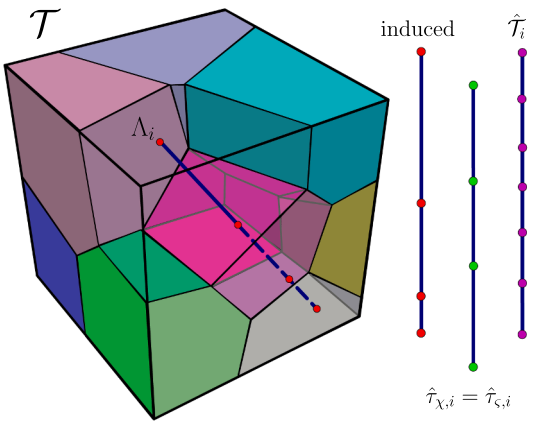
where, for $j \ge 2$ and $n = 1$, we take $\psi_\varsigma^{n-1} = \psi_\varsigma(t_{j-1})$, while for $j = 1$ and $n = 1$, $\psi_\varsigma^{n-1} = \psi_\varsigma(t_0) = g_{\varsigma,0}$, according to (3).

4.3. Space discretization of the constraint equations

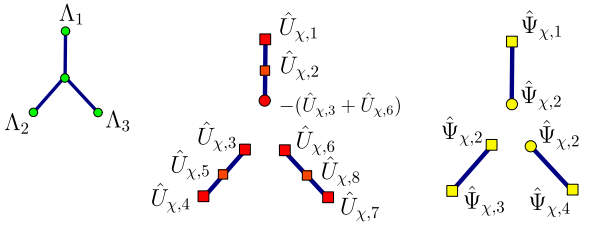
For the discretization of the 3D-1D coupled problem, we extend the 3D soil domain $\mathcal{D}^j$ to the whole Ω, and we consider a decomposition of $\mathcal{T}$ of Ω into non overlapping polyhedrons E which satisfy standard mesh assumptions [49]. We denote by $\mathcal{F}_E$ and $\mathcal{E}_E$ the set of faces and of edges of a generic polytope E. Finally, we fix $\mathcal{F} = \bigcup_{E\in\mathcal{T}} \mathcal{F}_E$.

Given an integer $k \ge 1$ and a polytope E, we denote by $\mathbb{P}_k^d(E)$ the space of polynomials in $\mathbb{R}^d$ of degree at most k on E, with $n_k^d = \dim \mathbb{P}_k^d(E) = \frac{(k+1)\dots(k+d)}{d!}$. We further adopt the standard convention $\mathbb{P}_{-1}^d(E) = \{0\}$ and $n_{-1}^d = 0$. Moreover, let us introduce the local polynomial projectors $\Pi_k^{\nabla,E} : H^1(E) \to \mathbb{P}_k^d(E)$, $\Pi_k^0 : L^2(E) \to \mathbb{P}_k^d(E)$, such that for any $q \in H^1(E)$

$$\left(\nabla q - \nabla\Pi_k^{\nabla,E} q, \nabla p\right)_E = 0 \quad \text{and} \quad \int_E \Pi_k^{\nabla,E} q = \begin{cases} \int_{\partial E} q & \text{if } k = 1, \\ \int_E q & \text{if } k \ge 2, \end{cases} \quad \forall p \in \mathbb{P}_k^d(E),$$



(a) Partitioning of a root segment induced by its intersections with the 3D mesh faces (red dots). The number of equispaced nodes used to discretize the 1D variables is a multiple of the number of these intersections.



(b) Xylem velocity and pressure head DOFs on a simplified RSA with three segments. Squares represent DOFs, whereas circles represent induced values for the related variable. More specifically, at the intersection point, two independent velocity DOFs ($\hat{U}_{\chi,3}$, $\hat{U}_{\chi,4}$) are defined; the velocity value associated with the circle ensures strong flux conservation. A single pressure head DOF ($\hat{\Psi}_{\chi,2}$) enforces continuity.

Fig. 3. Meshes and degrees of freedom (DOFs) on root segments.

and for any $q \in L^2(E)$

$$\left(q - \Pi_k^{0,E} q, p\right)_E = 0, \quad \forall p \in \mathbb{P}_k^d(E).$$

For each face $F \in \mathcal{F}$, we first introduce the space

$$\mathbb{B}(\partial F) = \left\{q \in C^0(\partial F) : q_{|e} \in \mathbb{P}_k^1(e)\ \forall e \in \mathcal{E}_F\right\},$$

which allows us to define the two-dimensional Virtual Element space as

$$\mathbb{W}(F) = \left\{q \in H^1(F) \cap C^0(F) : q_{|\partial F} \in \mathbb{B}(\partial F),\ \Delta q \in \mathbb{P}_k^2(F),\ \left(q - \Pi_k^{\nabla,F} q, p\right)_F = 0\ \forall p \in \mathbb{P}_k^2(F) \setminus \mathbb{P}_{k-2}^2(F)\right\},$$

where $\mathbb{P}_k^2(F) \setminus \mathbb{P}_{k-2}^2(F)$ denotes the set of two-dimensional polynomials defined on F of order $k-1$ or k. For each polyhedron $E \in \mathcal{T}$ we consider the boundary space

$$\mathbb{U}(\partial E) = \left\{q \in C^0(\partial E) : q_{|F} \in \mathbb{W}(F)\ \forall F \in \mathcal{F}_E\right\},$$

and the three-dimensional virtual element space

$$\mathbb{Q}_\varsigma(E) = \{q \in H^1(E) : q_{|\partial E} \in \mathbb{U}(\partial E),\ \Delta q \in \mathbb{P}_k^3(E),\ \left(q - \Pi_k^{\nabla,E} q, p\right)_E = 0\ \forall p \in \mathbb{P}_k^3(E) \setminus \mathbb{P}_{k-2}^3(E)\}.$$

Gluing together the local spaces, we define the global Virtual Element space for the soil pressure variable as [49]

$$\mathbb{Q}_\varsigma = \{q \in H_0^1(\Omega) \cap C^0(\Omega) : q \in \mathbb{Q}_\varsigma(E)\ \forall E \in \mathcal{T}\ \}.$$

Denoting by $\mathcal{P}_k^2(F)$ and $\mathcal{P}_k^3(E)$, suitable polynomial bases for $\mathbb{P}_k^2(F)$ and $\mathbb{P}_k^3(E)$, respectively, for each $Q_\varsigma \in \mathbb{Q}_\varsigma$, we choose the following degrees of freedom (for more details see [50,51]):

- the values of Q_ς at the vertices of $\mathcal{T}$;
- the values of Q_ς at the $k-1$ internal Gauss-Lobatto quadrature points on each internal edge of $\mathcal{T}$;
- the internal moments on each internal face $F \in \mathcal{F}$ defined as

$$\frac{1}{|F|} \int_F Q_\varsigma\ p \qquad \forall p \in \mathcal{P}_{k-2}^2(F); \tag{48}$$

- the internal moments on each element $E \in \mathcal{T}$ defined as:

$$\frac{1}{|E|} \int_E Q_\varsigma\ p \qquad \forall p \in \mathcal{P}_{k-2}^3(E) \quad \forall E \in \mathcal{T}. \tag{49}$$

In the following, we denote by $\{\varphi_{\varsigma,\alpha}^{\Psi}\}_{\alpha=1}^{N_\varsigma^\Psi}$ the set of Lagrangian basis functions associated with these degrees of freedom and spanning $\mathbb{Q}_\varsigma$.

Concerning the 1D variables, we can build on each segment Λ_i^j, for all $i \in \mathcal{Y}^j$, three possibly independent meshes $\widehat{\mathcal{T}}_i$, $\hat{\tau}_{\chi,i}$ and $\hat{\tau}_{\varsigma,i}$. Specifically, $\widehat{\mathcal{T}}_i$ is used for the discrete approximation of the xylem velocity $\hat{u}_\chi$ and of the xylem pressure head $\hat{\psi}_\chi$ on the segment Λ_i^j for all $j \geq 0$. On the other hand, the meshes $\hat{\tau}_{\chi,i}$ and $\hat{\tau}_{\varsigma,i}$ are used for the discretization of the xylem and soil control variables $\hat{\phi}_\chi$ and

$\widehat{\phi}_\varsigma$ on Λ_i^j, again for all $j \geq 0$. In the simulations, we typically use uniformly spaced partitions of the root segments. The number of nodes is set as a fixed multiple of the number of intersections between the considered root segment and the surrounding 3D mesh, as illustrated in Fig. 3a. For the sake of simplicity, we usually consider $\hat{\tau}_{\chi,i} = \hat{\tau}_{\varsigma,i}$. Discrete global spaces for the xylem velocity and pressure head are defined as

$$\widehat{\mathbb{V}}_\chi = \{\hat{v} \in \widehat{\mathcal{V}}_\chi : \hat{v}_{|e} \in \mathbb{P}_{k+1}(e)\ \forall e \in \widehat{\mathcal{T}}_i, \forall i \in \mathcal{Y}^j\}, \tag{50}$$

$$\widehat{\mathbb{Q}}_\chi = \{\hat{q} \in \widehat{\mathcal{Q}}_\chi : \hat{q}_{|e} \in \mathbb{P}_k(e)\ \forall e \in \widehat{\mathcal{T}}_i,\ \forall i \in \mathcal{Y}^j\}. \tag{51}$$

For elements $\widehat{V}_\chi \in \widehat{\mathbb{V}}_\chi$, we choose the following degrees of freedom:

- the value of $\widehat{V}_{\chi,i}$ at each internal vertex of $\widehat{\mathcal{T}}_i$, $\forall i \in \mathcal{Y}^j$, at the collar and at the root tips;
- $\#\mathcal{Y}_b^j - 1$ values of $\widehat{V}_{\chi,i}$, $i \in \mathcal{Y}_b^j$, at each intersection point $\boldsymbol{x}_b = \lambda(s_b)$, $b \in \mathcal{B}^j$. Let us indeed remark that the value that is left out can be retrieved from the others, according to (40), as depicted in Fig. 3b;
- if $k > 1$, for each $e \in \widehat{\mathcal{T}}_i$, $\forall i \in \mathcal{Y}^j$, we consider the scaled moments

$$\frac{1}{|e|}\int_e \widehat{V}_{\chi,i}\ \hat{g}^\nabla, \quad \forall \hat{g}^\nabla \in \nabla\mathcal{P}_k^1(e), \tag{52}$$

where $\mathcal{P}_k^1(e)$ is a suitable polynomial basis for $\mathbb{P}_k^1(e)$, and $\nabla\mathcal{P}_k^1(e)$ denotes the set containing the gradients of the basis functions in $\mathbb{P}_k^1(e)$. We denote by $\{\widehat{\varphi}^u_{\chi,\alpha}\}_{\alpha=1}^{\widehat{N}^u_\chi}$ the set of Lagrangian basis functions associated to the chosen degrees of freedom and spanning $\widehat{\mathbb{V}}_\chi$.

Let us now turn our attention to the xylem pressure head space. For each element $\widehat{Q}_\chi \in \widehat{\mathbb{Q}}_\chi$ we choose as degrees of freedom:

- the value of $\widehat{Q}_{\chi,i}$ at each internal vertex of $\widehat{\mathcal{T}}_i$, for all $i \in \mathcal{Y}^j$, at the collar and at the root tips;
- one single value of $\widehat{Q}_{\chi,i}$ at each intersection point $\boldsymbol{x}_b$, since we are assuming the continuity of the pressure (see Fig. 3b);
- if $k > 1$, the values at the $k-1$ internal Gauss-Lobatto quadrature points on each element of $\widehat{\mathcal{T}}_i$, for all $i \in \mathcal{Y}^j$.

The set of Lagrangian basis functions associated with the chosen degrees of freedom and spanning $\widehat{\mathbb{Q}}_\chi$ is denoted by $\{\widehat{\varphi}^\psi_{\chi,\alpha}\}_{\alpha=1}^{\widehat{N}^\psi_\chi}$.

For the control variables $\widehat{\phi}_\varsigma$ and $\widehat{\phi}_\chi$ we define the spaces $\widehat{\mathbb{Q}}^\phi_\varsigma$ and $\widehat{\mathbb{Q}}^\phi_\chi$ in a similar fashion to what was done for the reduced xylem pressure variable, and we denote by $\{\widehat{\varphi}^\phi_{\varsigma,\alpha}\}_{\alpha=1}^{\widehat{N}^\phi_\varsigma}$ and $\{\widehat{\varphi}^\phi_{\chi,\alpha}\}_{\alpha=1}^{\widehat{N}^\phi_\chi}$ the respective set of associated Lagrangian basis functions.

Remark 2. For ease of notation, we assume the same order of accuracy for the 3D and the 1D variables, as well as for the control variables. However, different orders of accuracy could also be employed.

From now on we will use uppercase symbols to refer to the space-discrete version of the quantities of interest. For instance,

$$\Psi_\varsigma = \sum_{\alpha=1}^{N^\psi_\varsigma} \Psi_{\varsigma,\alpha}\varphi^\psi_{\varsigma,\alpha}, \quad \widehat{\Psi}_\chi = \sum_{\alpha=1}^{\widehat{N}^\psi_\chi} \widehat{\Psi}_{\chi,\alpha}\widehat{\varphi}^\psi_{\chi,\alpha}, \quad \widehat{U}_\chi = \sum_{\alpha=1}^{\widehat{N}^u_\chi} \widehat{U}_{\chi,\alpha}\widehat{\varphi}^u_{\chi,\alpha},$$
$$\widehat{\Phi}_\varsigma = \sum_{\alpha=1}^{\widehat{N}^\phi_\varsigma} \widehat{\Phi}_{\varsigma,\alpha}\varphi^\psi_{\varsigma,\alpha}, \quad \widehat{\Phi}_\chi = \sum_{\alpha=1}^{\widehat{N}^\phi_\chi} \widehat{\Phi}_{\chi,\alpha}\widehat{\varphi}^\phi_{\chi,\alpha}$$

will denote the discrete version of ψ_ς, ψ_χ, $\hat{u}_\chi$, ϕ_ς, and ϕ_χ, respectively. With an abuse of notation, we will use the same uppercase symbol to refer to the vector containing the values assigned to the degrees of freedom of the corresponding discrete variable, the meaning being clear from the context.

Remark 3. The number of degrees of freedom for all the 1D variables actually depends on $j = 1, \dots, J$. However, we decide to drop the index j, since we are focusing on the time and space variation of the quantities as $t \in \mathcal{I}_j$, assuming j to be fixed.

On each element $E \in \mathcal{T}$ and for each $Z_\varsigma \in \mathbb{Q}_\varsigma$, as in [52,53], we define the following local discrete bilinear forms

$$\tilde{a}^E(\Psi_\varsigma, Q_\varsigma; Z_\varsigma) = \Big(K(\Pi_k^{0,E}Z_\varsigma)\Pi_{k-1}^{0,E}\nabla\Psi_\varsigma, \Pi_{k-1}^{0,E}\nabla Q_\varsigma\Big)_E + S^{\tilde{a},E}\Big(\Psi_\varsigma - \Pi_k^{\nabla,E}\Psi_\varsigma, Q_\varsigma - \Pi_k^{\nabla,E}Q_\varsigma; Z_\varsigma\Big),$$
$$\tilde{c}^E(\Psi_\varsigma, Q_\varsigma; Z_\varsigma) = \Big(C(\Pi_k^{0,E}Z_\varsigma)\Pi_k^{0,E}\Psi_\varsigma, \Pi_k^{0,E}Q_\varsigma\Big)_E + S^{\tilde{c},E}\Big(\Psi_\varsigma - \Pi_k^{0,E}\Psi_\varsigma, Q_\varsigma - \Pi_k^{0,E}Q_\varsigma; Z_\varsigma\Big),$$

where $S^{\tilde{a},E}(\cdot,\cdot;Z_\varsigma)$ and $S^{\tilde{c},E}(\cdot,\cdot;Z_\varsigma)$ are any computable, symmetric and positive definite bilinear forms such that $\tilde{a}^E(\cdot,\cdot;Z_\varsigma)$ and $\tilde{c}^E(\cdot,\cdot;Z_\varsigma)$ scale like their continuous counterparts [10]

$$a^E(\Psi_\varsigma, Q_\varsigma; Z_\varsigma) = \big(K(Z_\varsigma)\nabla\Psi_\varsigma, \nabla Q_\varsigma\big)_E, \quad c^E(\Psi_\varsigma, Q_\varsigma; Z_\varsigma) = \big(C(Z_\varsigma)\Psi_\varsigma, Q_\varsigma\big)_E,$$

respectively. We then define the matrices

$$\mathbf{A}(\Psi_\varsigma^n) \in \mathbb{R}^{N^\psi_\varsigma \times N^\psi_\varsigma} : \quad [\mathbf{A}(\Psi_\varsigma^n)]_{\alpha\beta} = \sum_{E\in\mathcal{T}} \tilde{a}^E\Big(\varphi^\psi_{\varsigma,\beta}, \varphi^\psi_{\varsigma,\alpha}; \Psi_\varsigma^n\Big),$$

$$\mathbf{C}(\Psi_\varsigma^n) \in \mathbb{R}^{N_\varsigma^\psi \times N_\varsigma^\psi} : \quad [\mathbf{C}(\Psi_\varsigma^n)]_{\alpha\beta} = \sum_{E\in\mathcal{T}} \tilde{c}^E\Big(\varphi_{\varsigma,\beta}^\psi, \varphi_{\varsigma,\alpha}^\psi; \Psi_\varsigma^n\Big),$$

where we again use the superscript n to refer to the value of the related discrete variable at time $t_{j,n}$. To work out the complete discrete matrix formulation of the constraint equations let us also define the matrices

$$\widehat{\mathbf{A}} \in \mathbb{R}^{\widehat{N}_\chi^u \times \widehat{N}_\chi^u} : \qquad [\widehat{\mathbf{A}}]_{\alpha\beta} = \Big(k_\chi \widehat{\varphi}_{\chi,\beta}^u, \widehat{\varphi}_{\chi,\alpha}^u\Big)_{\Lambda^j}, \tag{53}$$

$$\widehat{\mathbf{B}} \in \mathbb{R}^{\widehat{N}_\chi^\psi \times \widehat{N}_\chi^u} : \qquad [\widehat{\mathbf{B}}]_{\alpha\beta} = -\pi R^2\left(\widehat{\varphi}_{\chi,\alpha}^\psi, \frac{\partial \widehat{\varphi}_{\chi,\beta}^u}{\partial s}\right)_{\Lambda^j}, \tag{54}$$

$$\widehat{\mathbf{M}}_\mu \in \mathbb{R}^{\widehat{N}_\chi^\psi \times \widehat{N}_\chi^\psi} : \qquad [\widehat{\mathbf{M}}_\mu]_{\alpha\beta} = 2\pi R\Big(\mu\widehat{\varphi}_{\chi,\beta}^\psi, \widehat{\varphi}_{\chi,\alpha}^\psi\Big)_{\Lambda^j}, \tag{55}$$

$$\mathbf{M}_\mu \in \mathbb{R}^{N_\varsigma^\psi \times N_\varsigma^\psi} : \qquad [\mathbf{M}_\mu]_{\alpha\beta} = 2\pi R\Big(\ \mu\ \varphi_{\varsigma,\beta}^\psi, \varphi_{\varsigma,\alpha}^\psi\Big)_{\Lambda^j} \tag{56}$$

$$\mathbf{S}_\mu^\varsigma \in \mathbb{R}^{N_\varsigma^\psi \times \widehat{N}_\chi^\phi} : \qquad [\mathbf{S}_\mu^\varsigma]_{\alpha\beta} = 2\pi R\Big(\mu\widehat{\varphi}_{\chi,\beta}^\phi, \varphi_{\varsigma,\alpha}^\psi\Big)_{\Lambda^j}, \tag{57}$$

$$\mathbf{S}_\mu^\chi \in \mathbb{R}^{\widehat{N}_\chi^\psi \times \widehat{N}_\varsigma^\phi} : \qquad [\mathbf{S}_\mu^\chi]_{\alpha\beta} = 2\pi R\Big(\mu\ \widehat{\varphi}_{\varsigma,\beta}^\phi, \widehat{\varphi}_{\chi,\alpha}^\psi\Big)_{\Lambda^j}, \tag{58}$$

and the vectors

$$\boldsymbol{f}_\varsigma(\Psi_\varsigma^n) \in \mathbb{R}^{N_\varsigma^\psi} : \qquad [\boldsymbol{f}_\varsigma(\Psi_\varsigma^n)]_\alpha = -\sum_{E\in\mathcal{T}}\Big(K(\Pi_k^{0,E}\Psi_\varsigma^n)\boldsymbol{e}_z, \Pi_{k-1}^{0,E}\nabla\varphi_{\varsigma,\alpha}^\psi\Big)_E,$$

$$\widehat{\boldsymbol{f}}_\chi \in \mathbb{R}^{\widehat{N}_\chi^u} : \qquad [\widehat{\boldsymbol{f}}_\chi]_\alpha = -\pi R^2\Big(\boldsymbol{e}_z \cdot \boldsymbol{e}_s, \widehat{\varphi}_{\chi,\alpha}^u\Big)_{\Lambda^j}.$$

The space-time discrete matrix formulation of the constraint Eqs. (33)–(35) can finally be written as

$$\Big[\mathbf{A}(\Psi_\varsigma^n) + \tfrac{1}{\Delta t}\mathbf{C}(\Psi_\varsigma^n) + \mathbf{M}_\mu\Big]\Psi_\varsigma^n - \mathbf{S}_\mu^\varsigma\widehat{\Phi}_\chi^n - \frac{1}{\Delta t}\mathbf{C}(\Psi_\varsigma^n)\Psi_\varsigma^{n-1} - \boldsymbol{f}_\varsigma(\Psi_\varsigma^n) = \mathbf{0}, \tag{59}$$

$$\begin{bmatrix}\widehat{\mathbf{A}} & \widehat{\mathbf{B}}^T\\ \widehat{\mathbf{B}} & -\widehat{\mathbf{M}}_\mu\end{bmatrix}\begin{bmatrix}\widehat{U}_\chi^n\\ \widehat{\Psi}_\chi^n\end{bmatrix} + \begin{bmatrix}\mathbf{0}\\ \mathbf{S}_\mu^\chi\end{bmatrix}\widehat{\Phi}_\varsigma^n = \begin{bmatrix}\widehat{\boldsymbol{f}}_\chi\\ \mathbf{0}\end{bmatrix}. \tag{60}$$

Remark 4. The size of the matrices (53)–(58) actually changes as the root network evolves. However, since we are allowing for the growth of the RSA but not for its remodeling or regression, we do not need to recompute the matrices at each time step. Indeed, by numbering correctly the degrees of freedom, we can update the matrices by concatenating the contributions of the new basis functions to the matrices computed at the previous time step.

4.4. The solving strategy

The discrete cost functional, to be minimized subject to the time-space discrete constraints (59)–(60), is derived from (38) by replacing the $\mathcal{H}_\Gamma$-norms with norms in $L^2(\Lambda^j)$. Namely, we introduce

$$\widetilde{\mathcal{J}}(\widehat{\Phi}_\varsigma^n, \widehat{\Phi}_\chi^n) = \frac{1}{2}\Big(\|\Psi_\varsigma^n(\widehat{\Phi}_\chi^n) - \widehat{\Phi}_\varsigma^n\|_{\Lambda^j}^2 + \|\widehat{\Psi}_\chi^n(\widehat{\Phi}_\varsigma^n) - \widehat{\Phi}_\chi^n\|_{\Lambda^j}^2\Big). \tag{61}$$

Its algebraic form can be obtained by collecting the integrals of the basis functions into matrices (see Appendix C).

Given a fixed $\mathcal{I}_j$, in each sub-interval $(t_{j,n-1}, t_{j,n}]$, $n = 1, \dots, N$, the non-linearities characterizing Eq. (59) are tackled using the Picard non-linear iterative method, which is a globally convergent method that has been extensively analyzed in the case of Richards equation [54]. At each non-linear iteration, indexed by $\ell \geq 1$, we introduce the matrix

$$\mathcal{A}^\ell = \Big[\mathbf{A}(\Psi_\varsigma^{n,\ell-1}) + \tfrac{1}{\Delta t}\mathbf{C}(\Psi_\varsigma^{n,\ell-1}) + \mathbf{M}_\mu\Big],$$

and the vector

$$\boldsymbol{f}^\ell = \frac{1}{\Delta t}\mathbf{C}(\Psi_\varsigma^{n,\ell-1})\Psi_\varsigma^{n-1} + \boldsymbol{f}_\varsigma(\Psi_\varsigma^{n,\ell-1}),$$

where $\Psi_\varsigma^{n,\ell-1}$ is the soil pressure head obtained at the non-linear step $\ell - 1$, and we rewrite the discrete constraint Eqs. (59)–(60) as

$$\mathcal{A}^\ell\Psi_\varsigma^{n,\ell} = \mathbf{S}_\mu^\varsigma\widehat{\Phi}_\chi^{n,\ell} + \boldsymbol{f}^\ell, \tag{62}$$

$$\begin{bmatrix}\widehat{\mathbf{A}} & \widehat{\mathbf{B}}^T\\ \widehat{\mathbf{B}} & -\widehat{\mathbf{M}}_\mu\end{bmatrix}\begin{bmatrix}\widehat{U}_\chi^{n,\ell}\\ \widehat{\Psi}_\chi^{n,\ell}\end{bmatrix} = \begin{bmatrix}\mathbf{0}\\ -\mathbf{S}_\mu^\chi\end{bmatrix}\widehat{\Phi}_\varsigma^{n,\ell} + \begin{bmatrix}\widehat{\boldsymbol{f}}_\chi\\ \mathbf{0}\end{bmatrix}. \tag{63}$$

We then solve the following constrained optimization problem:

$$\begin{aligned}&\textit{Find } (\Psi_\varsigma^{n,\ell}, \widehat{U}_\chi^{n,\ell}, \widehat{\Psi}_\chi^{n,\ell}, \widehat{\Phi}_\varsigma^{n,\ell}, \widehat{\Phi}_\chi^{n,\ell}) \in \mathbb{Q}_\varsigma \times \widehat{\mathbb{V}}_\chi \times \widehat{\mathbb{Q}}_\chi \times \widehat{\mathbb{Q}}_\varsigma^\phi \times \widehat{\mathbb{Q}}_\chi^\phi\\ &\quad\textit{such that } \widetilde{\mathcal{J}}(\widehat{\Phi}_\varsigma^{n,\ell}, \widehat{\Phi}_\chi^{n,\ell}) \textit{ is minimized subject to (62)-(63).}\end{aligned} \tag{64}$$

Algorithm 1: The Solving Strategy.

Data: $\Psi_\varsigma^0,\ \Lambda^0$; /* Initial conditions */
for $j = 1, \dots, J$ **do**
  $\Lambda^j \leftarrow \text{Evolve}(\Lambda^{j-1}, \Psi_\varsigma^{j-1}, \Theta^{j-1}, \nabla\Theta^{j-1})$;
  for $n = 1, \dots, N$ **do**
    $\ell \leftarrow 0$;
    $\Psi_\varsigma^n \leftarrow \Psi_\varsigma^{n-1}$;
    while *non-linear stopping criteria is not satisfied* **do**
      Set an initial guess for control variables $\mathcal{X}_0$;
      $\begin{bmatrix}\widehat{\Phi}_\varsigma^{n,\ell}\\ \widehat{\Phi}_\chi^{n,\ell}\end{bmatrix} = \mathcal{X} = \text{CG}(\mathcal{X}_0)$; /* Solve (66) via the CG */
      Compute $\Psi_\varsigma^{n,\ell}(\widehat{\Phi}_\chi^{n,\ell})$ and $\begin{bmatrix}\widehat{U}_\chi^{n,\ell}(\widehat{\Phi}_\varsigma^{n,\ell})\\ \widehat{\Psi}_\chi^{n,\ell}(\widehat{\Phi}_\chi^{n,\ell})\end{bmatrix}$ from the systems in Eqs. (62)-(63);
      $\ell = \ell + 1$;
    end
  end
  $\Psi_\varsigma^0 \leftarrow \Psi_\varsigma^{N,\ell}$;
end

The constrained optimization problem (64) can actually be recast into an unconstrained optimization problem: $\Psi_\varsigma^{n,\ell}$ and $\widehat{\Psi}_\chi^{n,\ell}$ can be written as functions of $\widehat{\Phi}_\varsigma^{n,\ell}$ and $\widehat{\Phi}_\chi^{n,\ell}$ according to (62)-(63), and substituted inside the discrete cost functional (61), yielding to

$$\widetilde{\mathcal{J}}(\widehat{\Phi}_\varsigma^{n,\ell}, \widehat{\Phi}_{\chi,h}^{n,\ell}) = \frac{1}{2}\left(\mathcal{X}^T \boldsymbol{\mathcal{M}} \mathcal{X} + 2\mathcal{X}^T \boldsymbol{d} + b\right), \tag{65}$$

with $\mathcal{X} = \left[(\widehat{\Phi}_\varsigma^{n,\ell})^T\ (\widehat{\Phi}_\chi^{n,\ell})^T\right]^T$. The definition of $\boldsymbol{\mathcal{M}}$, $\boldsymbol{d}$ and b can be found in Appendix C. What it is worth underlining is that $\boldsymbol{\mathcal{M}}$ is a symmetric and positive semi-definite matrix. In [43] it has been formally shown that it is symmetric positive definite for the linear and stationary case. Thus, assuming the non-singularity of matrix $\boldsymbol{\mathcal{M}}$, the unconstrained problem (65) can be solved via the Conjugate Gradient method (CG in short), looking for the solution of the linear system

$$\nabla\widetilde{\mathcal{J}}(\mathcal{X}) = \boldsymbol{\mathcal{M}}\mathcal{X} + \boldsymbol{d} = \boldsymbol{0}. \tag{66}$$

Let us remark that the CG-solution of system (66) can be computed without explicitly assembling the matrix $\boldsymbol{\mathcal{M}}$. The action of $\boldsymbol{\mathcal{M}}$ on the descent direction $\delta\mathcal{X}$ can indeed be computed by solving independent sub-problems involving the 3D and 1D variables separately (see Appendix C for details). This is especially beneficial in simulations with a large number of root segments, where the decoupling of the sub-problems enables efficient parallelization and ensures scalability.

To reduce the number of iterations required by the conjugate gradient scheme a suitable preconditioning strategy could be devised. We refer to Section 6.3 in the numerical examples for details.

The whole solving process, accounting both for root growth and for the evolution of the quantities of interest is summarized in Algorithm 1. The function $\text{Evolve}(\Lambda^{j-1}, \Psi_\varsigma^{j-1}, \Theta^{j-1}, \nabla\Theta^{j-1})$ updates the current root system architecture Λ^{j-1} with the information given by the discrete soil pressure head Ψ_ς^{j-1} and by the discrete water content Θ^{j-1} and its gradient at time t_{j-1}, according to the RSA growth strategy introduced in Section 4.1 and detailed in Appendix A. Since we are using a Virtual Element method to discretize the soil pressure head, we need to resort to the L^2-projection operator defined on the elements $E \in \mathcal{T}$ to access the point-wise evaluation of Ψ_ς^{j-1} [55]. Thus, we actually approximate $\Psi_\varsigma^{j-1}(\boldsymbol{x})$, $\Theta^{j-1}(\boldsymbol{x})$ and $\nabla\Theta^{j-1}(\boldsymbol{x})$ in a point $\boldsymbol{x} \in \Omega$ with the weighted sums

$$\Psi_\varsigma^{j-1}(\boldsymbol{x}) \approx \frac{1}{\overline{\omega}(\boldsymbol{x})} \sum_{E\in\mathcal{T}:\boldsymbol{x}\in E} \omega_E \Pi_k^{0,E}(\Psi_\varsigma^{j-1}(\boldsymbol{x})),$$
$$\Theta^{j-1}(\boldsymbol{x}) \approx \frac{1}{\overline{\omega}(\boldsymbol{x})} \sum_{E\in\mathcal{T}:\boldsymbol{x}\in E} \omega_E\ \Theta\Big(\Pi_k^{0,E}(\Psi_\varsigma^{j-1}(\boldsymbol{x}))\Big),$$
$$\nabla\Theta^{j-1}(\boldsymbol{x}) \approx \frac{1}{\overline{\omega}(\boldsymbol{x})} \sum_{E\in\mathcal{T}:\boldsymbol{x}\in E} \omega_E\ C\Big(\Pi_k^{0,E}\Psi_\varsigma^{j-1}(\boldsymbol{x})\Big)\Pi_{k-1}^{0,E}(\nabla\Psi_\varsigma^{j-1}(\boldsymbol{x})),$$

where we choose as weights $\omega_E = |E|$, for each $E \in \mathcal{T}$, and $\overline{\omega}(\boldsymbol{x}) = \sum_{E\in\mathcal{T}:\boldsymbol{x}\in E} \omega_E$.

5. Modeling negative thigmotropic responses to physical barriers

Generally, roots are negative thigmotropic, meaning that they have the tendency to grow away from physical obstacles. Accurately modeling this behavior poses significant computational challenges. A common strategy in the literature is based on monitoring the

position of the tip with respect to the obstacle surface by means of a signed distance function and subsequently correct the root tip position in case intrusion has occurred [14,56]. However, this iterative correction can become computationally demanding, especially when there are a large number of closely spaced obstacles or numerous root tips.

Here, we propose a different approach that consists of modeling the tip growth field $\boldsymbol{w}_P^j$ defined in (45) as follows. Let us denote by $\mathcal{B}$ the boundary of an obstacle and let $d_{\mathcal{B}}(\boldsymbol{x})$ be a given distance function measuring the distance from $\mathcal{B}$. Let us then define the *repulsion function*

$$\eta(\boldsymbol{x}) := \begin{cases} \dfrac{d_{\max} - d_{\mathcal{B}}(\boldsymbol{x})}{d_{\max}} & \text{if } d_{\mathcal{B}}(\boldsymbol{x}) \le d_{\max}, \\ 0 & \text{otherwise,} \end{cases} \tag{67}$$

and

$$\boldsymbol{r}_P := \begin{cases} -\dfrac{\nabla\eta(\boldsymbol{x}_P)}{\|\nabla\eta(\boldsymbol{x}_P)\|} & \text{if } d_{\mathcal{B}}(\boldsymbol{x}_P) < d_{\max}, \\ \boldsymbol{0} \in \mathbb{R}^3 & \text{otherwise.} \end{cases}$$

The vector field $\boldsymbol{w}_P^j$ is defined as

$$\boldsymbol{w}_P^j := V_P^j \frac{(1-\eta^2(\boldsymbol{x}_P))\boldsymbol{d}_P^j + \eta^2(\boldsymbol{x}_P)\boldsymbol{r}_P}{||(1-\eta^2(\boldsymbol{x}_P))\boldsymbol{d}_P^j + \eta^2(\boldsymbol{x}_P)\boldsymbol{r}_P||}, \tag{68}$$

where V_P^j ([cm day^{-1}]) is the growth rate, and $\boldsymbol{d}_P^j$ is the standard growth direction that summarizes typical plant tropisms. Both the rate V_P^j and the direction $\boldsymbol{d}_P^j$ depend on the computed soil water pressure head and water content, as well as on a set of parameters accounting for plant genetics and soil type, as stated in the growth law (45). The definitions of V_P^j and $\boldsymbol{d}_P^j$ are based on a combination of several existing standardized approaches (see, for example, [8,15,18,57]) and are detailed in Appendix A.

According to (68), standard growth tendency dominates when $\eta(\boldsymbol{x}_P) \ll 1$, while when $\eta(\boldsymbol{x}_P) \sim 1$, i.e., when the root tip is close to an obstacle or barriers, the growth direction is almost completely deviated, preventing the roots from penetrating the barrier. The parameter $d_{\max}$, as well as the shape of the repulsion function, need to be carefully calibrated to avoid early or late deviation. The optimal configuration should be chosen based on phenomenological observations and adapted to the mesh resolution and the expected maximum elongation rate of the specific plant root.

In the numerical experiments, we treat the repulsion function (67) as a VEM function of order $k = 1$ over Ω. We observe that this function is completely determined by assigning its values at the mesh vertices. In particular, we assign a value of 1 at vertices located on the impenetrable domain boundaries and zero elsewhere. As a consequence, the value of $d_{\max}$ in (67) is determined for us by the resolution of the tessellation. We note that on generally shaped elements, the function may assume negative values, see [55], which can be easily flattened to zero.

Our method shares certain similarities with the approach proposed in [8], which introduces an alternative function for root deviation. However, in this case, obstacles are modeled as regions with a very stiff substrate, and the natural root response is weakened during root-obstacle interactions. A key difference is that, in our case, by exploiting the flexibility of virtual element methods, we do not solve the governing equations inside the obstacles, avoiding numerical instabilities that may arise from modeling material heterogeneity.

6. Numerical results

In this section, we propose some numerical examples to validate the proposed approach. Given $E \in \mathcal{T}$, we denote by $h_E := \mathrm{diam}(E)$ the diameter of E, and we set $h = \max_{E\in\mathcal{T}} h_E$. The refinement level of the 1D partitions is instead given in relation to the refinement level of the mesh induced on each Λ_i^j by the intersection with the polyhedrons in $\mathcal{T}$ (see Section 4.3). We hence introduce three parameters $\hat{\delta}_i$, $\hat{\delta}^{\phi}_{\chi,i}$ and $\hat{\delta}^{\phi}_{\varsigma,i}$, which express the ratio between the number of elements in $\widehat{\mathcal{T}}_i$, $\hat{\tau}_{\chi_i}$ and $\hat{\tau}_{\varsigma,i}$ and the number of elements of the mesh induced on Λ_i^j. For simplicity, in the proposed numerical examples we always consider equispaced partitions and we choose unique values of the 1D mesh parameters for the different root segments. In particular $\hat{\delta}_i = 1$, and $\hat{\delta}^{\phi}_{\chi,i} = \hat{\delta}^{\phi}_{\varsigma,i} = 0.5$, $\forall i = 1, \dots, J$. For what concerns the order of accuracy we choose $k = 1$ for all the variables.

6.1. Test problem 1 (TP1): Convergence results

Let us consider a cubic domain $\Omega = (-1, 1)^3$ and let Σ be a straight root segment crossing Ω from side to side. In particular, Σ coincides with a cylinder of radius $R = 10^{-2}$ and height 2 whose centerline lies on the z-axis. In this numerical test, we are not accounting for root growth: we consider instead a simplified configuration with a known analytical solution, to analyze accuracy.

The considered test problem is adapted from Test Problem 1 in [43], which is modified by introducing time dependency and non-linearity. In particular, we aim at solving the following 3D-1D coupled problem for $t \in (0, 1]$

$$\begin{cases} \left(C(\psi_\varsigma)\frac{\partial \psi_\varsigma}{\partial t}, q_\varsigma\right)_D + \left(K(\psi_\varsigma)\nabla\psi_\varsigma, \nabla q_\varsigma\right)_D + \left(2\pi R\mu(\widehat{\psi}_\varsigma - \widehat{\psi}_\chi), \widehat{q}_\varsigma\right)_\Lambda = \left(S, q_\varsigma\right)_D & \forall q_\varsigma \in \mathcal{Q}_\varsigma, \\ \left(k_\chi \widehat{u}_\chi, \widehat{v}_\chi\right)_\Lambda - \left(\widehat{\psi}_\chi, \pi R^2 \frac{\partial \widehat{v}_\chi}{\partial s}\right)_\Lambda = \pi R^2 \left[(\widehat{S}_\psi \widehat{v}_\chi)_{|[0,0,1]^T} - (\widehat{S}_\psi \widehat{v}_\chi)_{|[0,0,-1]^T}\right] & \forall \widehat{v}_\chi \in \widehat{\mathcal{V}}_\chi, \\ \left(\pi R^2 \frac{\partial \widehat{u}_\chi}{\partial s}, \widehat{q}_\chi\right)_\Lambda + \left(2\pi R\mu(\widehat{\psi}_\chi - \widehat{\psi}_\varsigma), \widehat{q}_\chi\right)_\Lambda = \left(\widehat{S}, \widehat{q}_\chi\right)_\Lambda & \forall \widehat{q}_\chi \in \widehat{\mathcal{Q}}_\chi, \end{cases} \tag{69}$$

with

$$C(\psi_\varsigma) = \frac{-\psi_\varsigma}{(1+\psi_\varsigma^2)^{3/2}} + 4, \quad K(\psi_\varsigma) = 1, \quad k_\chi = \pi R^2 \left(\frac{z^2}{3} + \frac{1}{2}\right)^{-1}, \quad \mu = \frac{2R}{R^2+2}.$$

Problem (69) is actually obtained from (33)–(37) by neglecting the gravity terms, introducing proper forcing terms S, $\widehat{S}$, imposing boundary Dirichlet conditions $\widehat{S}_\psi$ for the xylem pressure head, and imposing initial and Dirichlet boundary conditions for the soil pressure head such that the exact solution of (69) is

$$\psi_\varsigma = \frac{1}{2}(x^2+y^2)(1-z^2) - 1 - t,$$
$$\widehat{\psi}_\chi = z^2 - 2 - t, \qquad \widehat{u}_\chi = -2z\left(\frac{z^2}{3} + \frac{1}{2}\right).$$

The accuracy of the method is measured by the following error indicators:

$$e^2_{L^2,\psi_\varsigma} = \frac{\sum_{E\in\mathcal{T}} \|\psi_\varsigma - \Pi^0_k \Psi_\varsigma\|^2_E}{\|\psi_\varsigma\|^2_\Omega}, \quad e_{L^2,\widehat{\psi}_\chi} = \frac{\|\widehat{\psi}_\chi - \widehat{\Psi}_\chi\|_\Lambda}{\|\widehat{\psi}_\chi\|_\Lambda},$$
$$e^2_{H^1,\psi_\varsigma} = \frac{\sum_{E\in\mathcal{T}} \|\nabla\psi_\varsigma - \Pi^0_{k-1}\nabla\Psi_\varsigma\|^2_E}{\|\nabla\psi_\varsigma\|^2_\Omega}, \quad e_{L^2,\widehat{u}_\chi} = \frac{\|\widehat{u}_\chi - \widehat{U}_\chi\|_\Lambda}{\|\widehat{u}_\chi\|_\Lambda}, \tag{70}$$

corresponding, respectively, to the relative errors in L^2-norm for the soil and xylem pressure head, in H^1-seminorm for the soil pressure head and in L^2-norm for the xylem velocity. Concerning the interface variables, we introduce two additional error indicators

$$e_{L^2,\widehat{\psi}_\varsigma} = \frac{\|\gamma_\Gamma \psi_\varsigma - \widehat{\Phi}_\varsigma\|_\Lambda}{\|\gamma_\Gamma \psi_\varsigma\|_\Lambda}, \quad e_{L^2,\widehat{\psi}_\chi} = \frac{\|\widehat{\psi}_\chi - \widehat{\Phi}_\chi\|_\Lambda}{\|\widehat{\psi}_\chi\|_\Lambda}, \tag{71}$$

which measure the L^2-distance of the control variables from the trace of the corresponding pressure head variable. We consider 4 different tetrahedral meshes, with mesh size $h \approx 4.67e\text{-}01, 3.56e\text{-}01, 2.82e\text{-}01, 2.33e\text{-}01$. Concerning the time-advancing scheme, let us remark that, since the exact pressure variables are linear in time, the proposed results can be obtained by performing just one backward Euler step, i.e., we set $\Delta t = 1$. Moreover, the setting of $\Delta\mathcal{I}$ is not necessary, as root growth is not considered in the test.

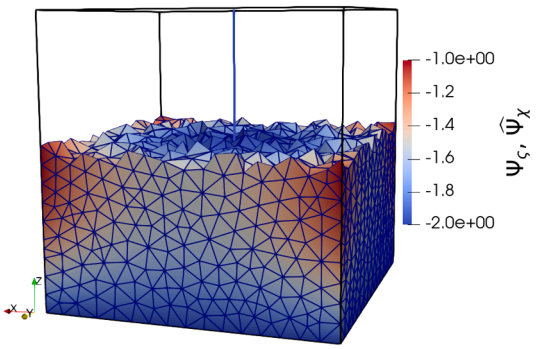
Fig. 4 shows the numerical solution of the problem obtained at $t = 1$ on the finest mesh. Fig. 4a reports the pressure head distribution in the soil sample and in the root segment, and it is obtained by a crinkle cut of the soil sample with a plane orthogonal to the z-axis to show the pressure distribution in the interior of the domain; 4b shows, instead, the velocity field, where the 3D velocity variable is reconstructed as

$$\widehat{U}_\chi \approx -\Pi^{0,E}_{k-1}\nabla\Psi_\varsigma \quad \forall E \in \mathcal{T},$$

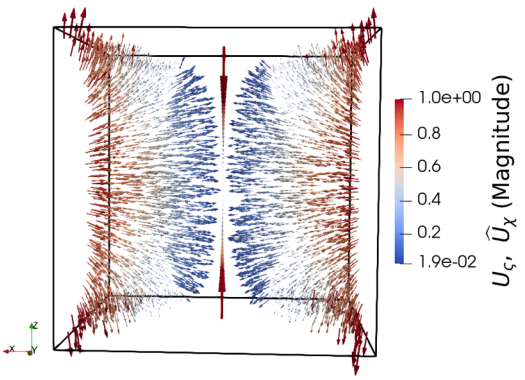
provided that $K(\psi_\varsigma) \equiv 1$ and that the gravity term is neglected.

Fig. 5 displays the convergence curves for the error indicators (70) and (71) as the related mesh parameters vary. In addition, Fig. 5 reports the Empirical Order of Convergence (EOC in short) measured for each variable. Fig. 5a refers to the soil error indicators, which appear to converge at the expected rate. Indeed, since we are using a primal formulation for the soil pressure variable, e_{L^2,ψ_ς} is expected to decay as $O(h^2)$, whereas e_{H^1,ψ_ς} as $O(h)$. For what concerns the xylem error indicators, let us observe that, since the 1D mesh parameters $\hat{\delta}$, $\hat{\delta}^\phi_\chi$, $\hat{\delta}^\phi_\varsigma$ are kept fixed, a finer 3D mesh induces finer 1D partitions. In particular we denote by $\hat{h}$, $\hat{h}^\phi_\chi$ and $\hat{h}^\phi_\varsigma$ the width of the equispaced intervals respectively of $\widehat{\mathcal{T}}$, $\widehat{\tau}_\chi$ and $\widehat{\tau}_\varsigma$ and we analyze the convergence of $e_{L^2,\widehat{\psi}_\chi}$ and $e_{L^2,\widehat{u}_\chi}$ with respect to $\hat{h}$, and of $e_{L^2,\widehat{\psi}_\chi}$ and $e_{L^2,\widehat{\psi}_\varsigma}$ with respect to $\hat{h}^\phi_\chi$ and $\hat{h}^\phi_\varsigma$, respectively. Actually, since we are considering $\hat{\delta}^\phi_\chi = \hat{\delta}^\phi_\varsigma$ we here have $\hat{h}^\phi := \hat{h}^\phi_\varsigma = \hat{h}^\phi_\chi$. Also in this case we can observe how xylem pressure head and velocity converge at the expected rate: indeed we expect both $e_{L^2,\widehat{\psi}_\chi}$ and $e_{L^2,\widehat{u}_\chi}$ to converge as $O(\hat{h}^2)$. For what concerns the control variables, we have no theoretical results. However, we observe an empirical convergence rate equal to 2 for both variables, which is quite predictable since they represent the finite element interpolation of their continuous counterparts.

Concerning the non-linearities and the conjugate gradient algorithm, we want to observe that, for each mesh refinement, Algorithm 1 stops after 8 non-linear iterations ℓ and, as ℓ increases, we observe a decrease in the number of CG iterations required to reach convergence, as shown in Table 1 for the finest mesh.



(a) Numerical pressure head. The view is obtained by a crinkle cut of the 3D domain with a plane orthogonal to the z-axis).



(b) Numerical velocity field.

Fig. 4. TP1: Numerical solution in the 3D soil sample and in the root segment at the final time $t = 1$ on the finest mesh.

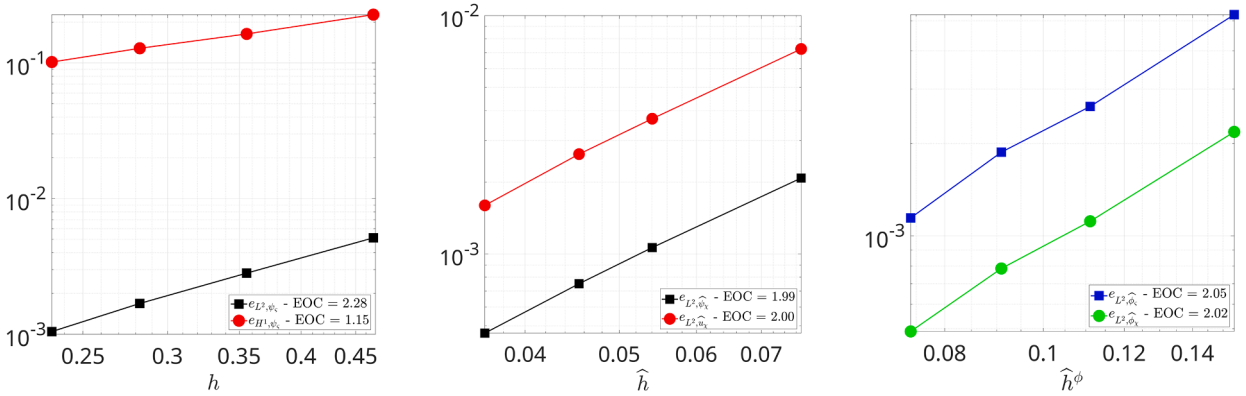


Fig. 5. TP1: Behaviour of the errors (70)-(71) as the related mesh parameter decreases at the final time $t = 1$.

Table 1
TP1: Number of CG iterations for each non-linear iteration ℓ for the finest mesh.

ℓ	0	1	2	3	4	5	6	7
# CG	22	20	16	12	9	5	2	0

6.2. Test problem 2 (TP2): Root architecture development in sealed soil sample

For this second numerical example we consider a small soil sample $\Omega = (0, B)^2 \times (-H, 0)$, with B =3 cm and H =6 cm. We assume the seed to be in position $\boldsymbol{x}_s = (1.5, 1.5, 0.1)$ cm, i.e., below the top surface of the soil sample, and to be connected to the upper face by a vertical mesocotyl. We do not aim at reproducing a specific plant genotype, but at testing the proposed 3D-1D coupling approach along with the RSA growth in a controlled setting, in which all the conditions are optimal for root growth.

We consider a uniform hexahedral mesh with size $h = 0.15$ cm, whereas we simulate root growth in a time span of 9 days, divided into uniform time intervals of width $\Delta\mathcal{I}_j = 0.2$ days. For the time discretization of the constraint equations we are not further subpartitioning the time steps $\mathcal{I}_j$ used for root growth, i.e., we choose $\Delta t = \Delta\mathcal{I}_j$, $\forall j \geq 1$ (see Section 4.2).

We assume the soil sample to be bounded into a box whose walls are impenetrable for the roots. From a practical standpoint, we treat the walls as an obstacle, defining a linear repulsion function η as the one in (67). In particular we set $\eta(\boldsymbol{x}) = 1$ for $\boldsymbol{x} \in \partial\Omega$ and we assume η to linearly decay from 1 to 0 within the first layer elements, i.e., at a distance h from the faces of Ω.

Similarly to [8], at the initial time $t_0 = 0$, we consider a linear soil pressure head increasing from $\Psi_\varsigma = -6$ cm at the top to $\Psi_\varsigma = 0$ cm at the soil bottom, as reported in Fig. 6. For each time $t > 0$ we set no flux boundary conditions on all the sample faces except for the bottom one, on which we keep a constant water table $\Psi_\varsigma = 0$ cm. At the root collar we set a constant transpiration rate of 0.2 cm^3/day.

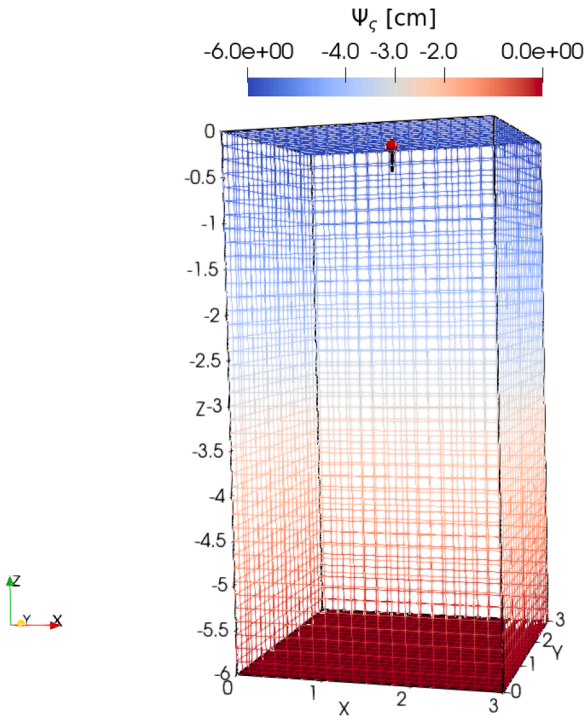


Fig. 6. TP2: Hexahedral mesh and (initial) soil pressure head distribution. The red face corresponds to the water table, whereas the red dot corresponds to the seed position $\boldsymbol{x}_S$.

Table 2
TP2: PDE parameters used for simulation.

Parameter	Value	Unit	Description	Reference
a	0.03	1/cm	Water retention curve shape parameter	[8]
n	2.5	–	Water retention curve shape parameter	[8]
θ_r	0.06	–	Residual volumetric water content	[8]
θ_s	0.41	–	Saturated volumetric water content	[8]
K_s	10.24	cm/day	Saturated hydraulic conductivity	[8]
R	0.05	cm	Root radius	[58]
k_x	0.18	day/cm	Reciprocal of specific root axial conductance	[8,22]
μ	$1.36 \cdot 10^{-6}$	cm^2/day	Permeability of root wall	[22]
$\sigma_{\max}$	1	MPa	Soil strength parameter	

At each time-step ΔT_j we solve a 3D-1D coupled problem in the form of (33)-(37) applying the solving strategy described in Section 4.4. In particular, we choose the Van Genuchten-Mualem model [26]

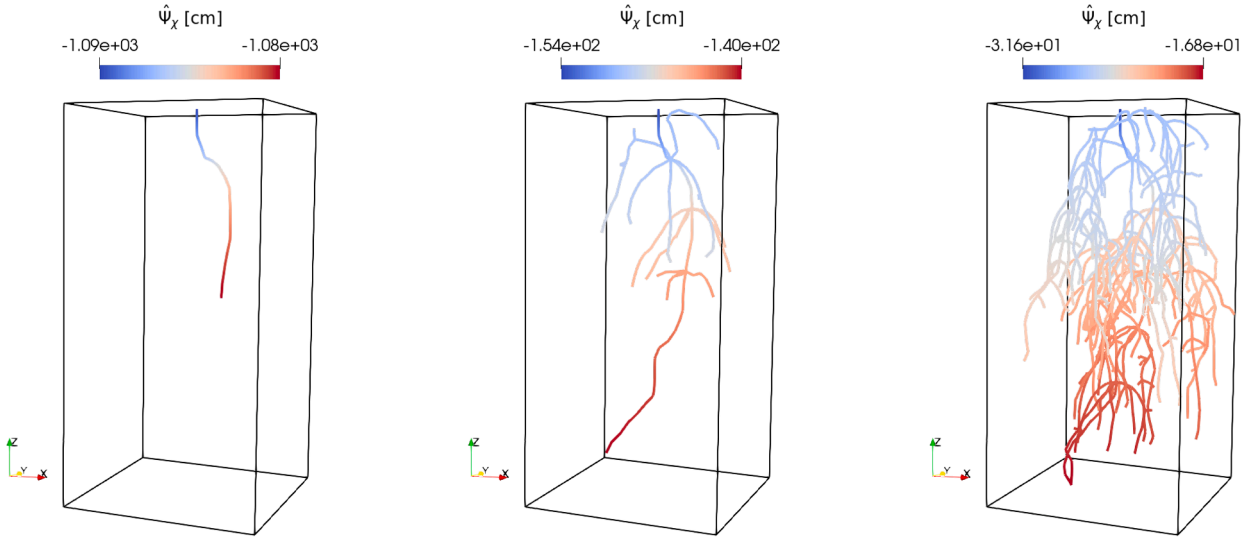
$$\theta(\psi_\varsigma) = \begin{cases} \theta_r + \frac{\theta_s - \theta_r}{\left[1+(a|\psi_\varsigma|)^n\right]^m} & \text{if } \psi_\varsigma < 0, \\ \theta_s & \text{if } \psi_\varsigma \geq 0, \end{cases} \quad \text{with } m = 1 - \frac{1}{n}, \tag{72}$$

$$K(\psi_\varsigma) = \begin{cases} K_s \frac{\left(1-(a|\psi_\varsigma|)^{n-1}[1+(a|\psi_\varsigma|)^n]^{-m}\right)^2}{\left[1+(a|\psi_\varsigma|)^n\right]^{\frac{m}{2}}} & \text{if } \psi_\varsigma < 0, \\ K_s & \text{if } \psi_\varsigma \geq 0, \end{cases} \tag{73}$$

$$C(\psi_\varsigma) = \begin{cases} anm\left(a|\psi_\varsigma|\right)^{n-1} \frac{\theta_s - \theta_r}{\left[1+(a|\psi_\varsigma|)^n\right]^{m+1}} & \text{if } \psi_\varsigma < 0, \\ 0 & \text{if } \psi_\varsigma \geq 0. \end{cases} \tag{74}$$

The value assigned to the parameters involved in (72)–(74) and in (33)–(37) are summarized in Table 2.

For what concerns the RSA growth parameters we refer to Appendix B.1. Fig. 7 reports the root network at three different time instants, namely for $t = 3, 6$ and 9 days, together with the xylem pressure head distribution. In Fig. 7c the effect of the repulsion



(a) $t = 3$ days. (b) $t = 6$ days. (c) $t = 9$ days.

Fig. 7. TP2: RSA at three different time instants.

function on the growth direction is particularly evident close to the bottom face of the domain, where the thigmotropic behavior of the primary root can be observed.

Concerning the soil variables, we notice from Fig. 8 that the velocity field is oriented in the radial direction around the roots, pointing towards the roots themselves. The figure shows the magnitude and orientation of the velocity field close to the primal root at $t = 3$ days. Since the soil flux is entering in roots, we can assert that the root water uptake $2R\pi\mu(\gamma_\Gamma\psi_\varsigma - \gamma_\Gamma\psi_\chi)$ is positive at that stage. However, one of the strengths of the optimization-based approach is that the approximation of the interface quantities $\gamma_\Gamma\psi_\varsigma$, $\gamma_\Gamma\psi_\chi$ is directly computed and stored in the auxiliary variables $\widehat{\Phi}_\varsigma$, $\widehat{\Phi}_\chi$, so that the water uptake along the RSA can easily be computed without the need of post-processing, at any time of the simulation.

Fig. 9-left shows the magnitude of the water uptake at $t = 9$ days. Due to the constant transpiration rate imposed, we observe that the roots near the root collar are primarily responsible for water uptake. This is a consequence of the fact that the permeability μ is assumed to be uniform across all root segments. Recent works have shown that older root segments can play an important role in water uptake [59]. However, in many scenarios, this process mostly occurs at the youngest root segments (the ones closest to the root tips), while the older ones are mainly responsible for the transport of water towards the collar. To reflect this behavior in the model, μ can be chosen as a decreasing function of time, and in particular of the age of the root segments. For simplicity, we here propose a case in which we set $\mu = 0$ for all the root segments Λ_i^j whose age a_i^j is greater than 3 days, i.e., for all the segments that have been existing for more than 3 days from the beginning of the simulation. Conversely, we impose μ as specified in Table 2 for root segments with $a_i^j < 3$ days. Fig. 9-right shows the water uptake resulting from this last setting. As expected, this adjustment increases the water uptake in the youngest root segments, which now exclusively sustain the imposed transpiration rate. On the other hand, older root segments, marked in purple in Fig. 9-right, no longer contribute to water uptake. It is worth noting that smoother dependencies of μ on segment age could be employed to better capture specific experimental observations.

6.3. Test problem 3 (TP3): Root architecture development in stony soil

This third numerical experiment examines root growth in a stony soil on a wider space and time scales with respect to the previous test case.

We consider a hexahedral soil sample $\Omega_{\text{soil}} := (0, B)^2 \times (-H, 0)$, with $B = 50$ cm and $H = 100$ cm, which contains two spherical stones

$$\Omega^i_{\text{stone}} := \{\boldsymbol{x} \in \mathbb{R}^3, \|\boldsymbol{x} - \boldsymbol{x}^i_{\text{stone}}\| \le r_i\}$$

with

$$\boldsymbol{x}^1_{\text{stone}} = [15, 15, -36.5] \text{ cm}, \quad r_1 = 5 \text{ cm},$$
$$\boldsymbol{x}^2_{\text{stone}} = [25, 31.25, -25] \text{ cm}, \quad r_2 = 6 \text{ cm}.$$

The spheres are discretized as *UV spheres*, which is a standard shape available in many 3D modeling tools. In particular, we tessellate the surface of the spheres along 8 meridians and 6 parallels each. Since the stones are assumed to be impervious, we exclude them from the computational domain, i.e. $\Omega = \Omega_{\text{soil}} \setminus \{\Omega^i_{\text{stone}}\}_{i\in\{1,2\}}$.

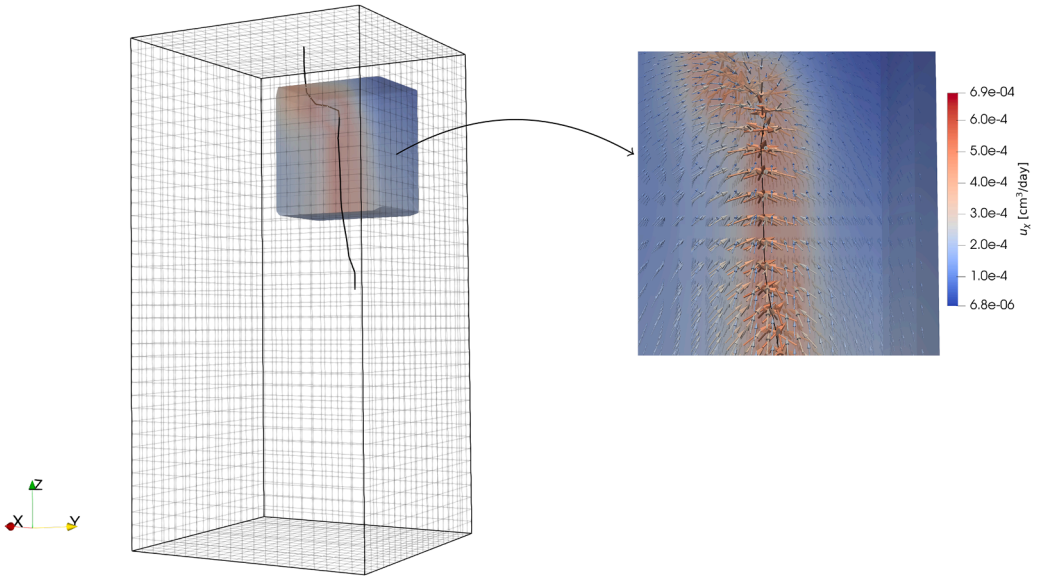


Fig. 8. TP2: Detail on 3D velocity field at $t = 3$ days in proximity of the RSA.

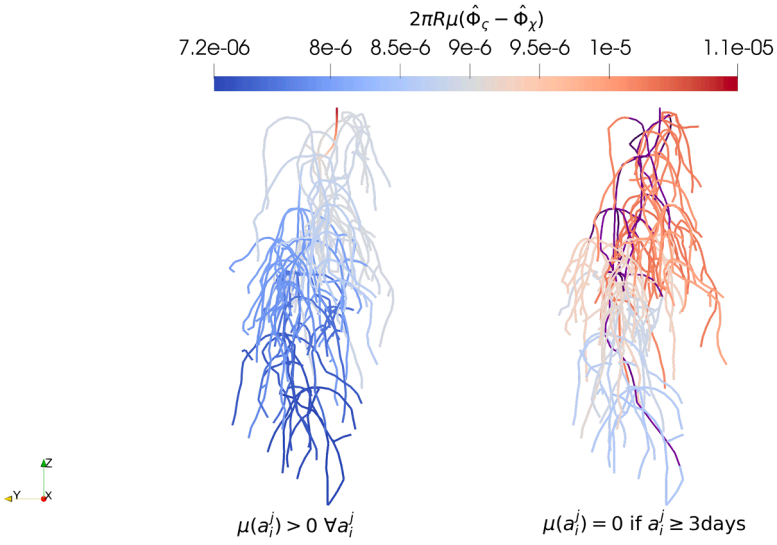
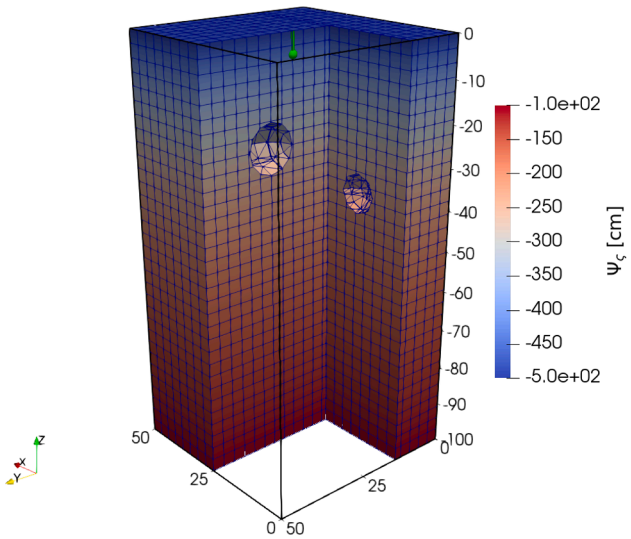


Fig. 9. TP2: Water uptake along the RSA. On the left: uptake occurs along the whole root network. On the right: uptake occurs only at root segments which are less than 3 days old; older root segments are marked in purple.

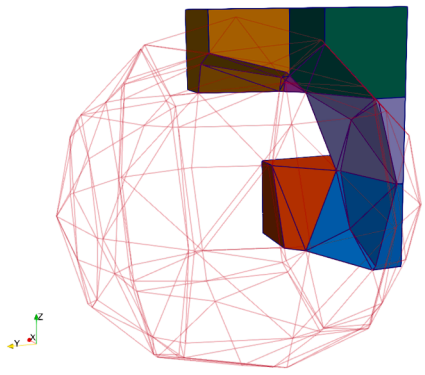
Mesh generation on Ω exploits the possibility of VEM to handle generic polyhedral cells. We begin by creating a regular 3D structured grid mesh for the Ω_{soil} domain, using cubes of edge 3.125 cm. Then, since the stones are not involved in the simulation, we subtract them from the mesh by removing the material from the 3D cells. The result of this process is shown in Fig. 10a, where part of the global domain mesh is clipped to reveal the internal removed cells, while the color scale refers to the initial soil water pressure head distribution. As we can observe from the image, the resulting mesh contains complex polyhedral cells, which can be easily handled by the numerical method proposed in this work. Fig. 10b illustrates a sample of the generated polyhedral cells, highlighting the presence of concave shapes. Using the VEM, such badly-shaped elements can easily be handled, without the need of generating good quality sub-tetrahedrons and without consequently refine the neighboring elements to keep conformity [17].

On the top and bottom faces of Ω we impose Dirichlet boundary conditions for the soil water pressure head ψ_ζ. In particular we set $\psi_\zeta = -500$ cm at the top and $\psi_\zeta = -100$ cm at the bottom. No flux boundary conditions are imposed on all the other faces, on the stone surface and at root tips, while we set a constant transpiration rate of $0.2\,\text{cm}^3/\text{day}$ at the root collar [8].

The initial condition for the soil water pressure head is obtained by solving (33) with $C(\psi_\zeta) = 0\ \forall \psi_\zeta$ and $\mu = 0$, i.e., by solving a stationary problem is absence of the RSA. We then simulate root growth in Ω for 160 days, starting from a seed positioned in $\boldsymbol{x}_S = [25, 25, -5]$ cm. We divide the considered time-span into uniform time intervals of width $\Delta\mathcal{I}_j = 1$ day. For the time discretization



(a) Clipped view of the 3D mesh. Color scale refers to the initial soil pressure head distribution. Seed and mesocotyl are colored in green.



(b) Sample of cells around Ω^1_{stone}.

Fig. 10. TP3: The three-dimensional mesh of the stony soil.

Table 3
TP3: PDE parameters used for simulation.

Parameter	Value	Unit	Description	Reference
a	0.02	1/cm	Water retention curve shape parameter	[60]
n	1.2	–	Water retention curve shape parameter	[60]
θ_r	0.06	–	Residual volumetric water content	[8,60]
θ_s	0.41	–	Saturated volumetric water content	[8,60]
K_s	10.24	cm/day	Saturated hydraulic conductivity	[8,60]
R	0.05	cm	Root radius	[58]
k_χ	0.18	day/cm	Reciprocal of specific root axial conductance	[8,22]
μ	$1.36 \cdot 10^{-6}$	cm^2/day	Permeability of root wall	[22]
$\sigma_{\max}$	1	MPa	Soil strength parameter	

of the constraint equations we choose $\Delta t = \Delta T_j$. The PDE parameters used in this simulation are reported in Table 3, whereas the water content $\theta(\psi_\varsigma)$ and the non-linear coefficients $K(\psi_\varsigma)$ and $C(\psi_\varsigma)$ are defined as in (72)–(74), respectively. With respect to the previous test case, we are choosing lower values of a and n. According to (72), this promotes root growth as it enhances water retention at high values of $|\psi_\varsigma|$.

The parameters governing the development of the RSA are reported in Appendix B.2. Fig. 11 shows the evolution of the RSA at different stages of the simulation, namely after 40, 80 and 160 days, along with the xylem pressure head distribution.

The root wall permeability was kept constant, but as in the previous numerical example it could be linked, for example, to the root age.

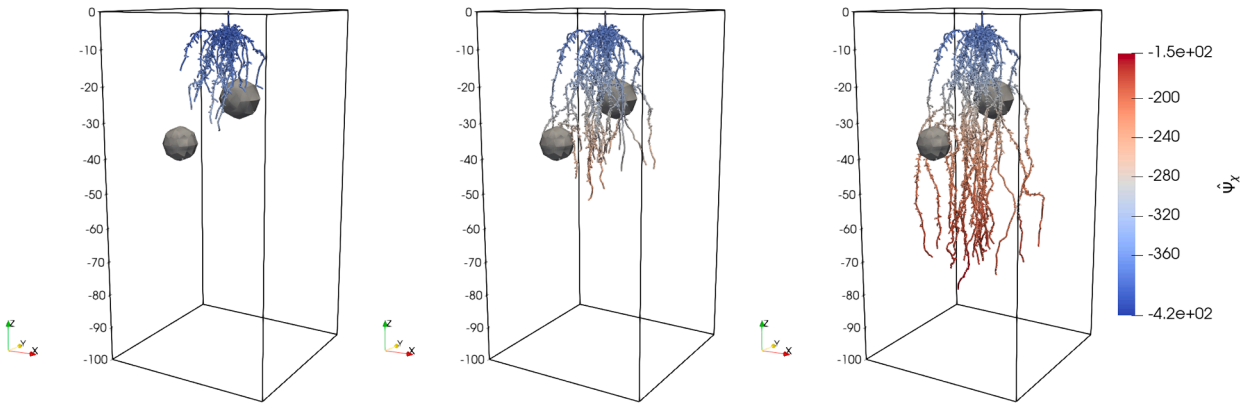
The contribution of the repulsion function in the computation of the growth direction allows us to avoid the roots to enter the stones. In particular, for the proposed experiment we defined a function $\eta(\boldsymbol{x})$ that varies linearly between 1 and 0 in the first layer of elements of a sub-tetrahedralization of $\mathcal{T}$ around the stones themselves, but the actual repulsion function was then defined as

$$\tilde{\eta}(\boldsymbol{x}) = \begin{cases} \eta(\boldsymbol{x}) & \text{if } \eta(\boldsymbol{x}) > 0.9 \\ 0 & \text{otherwise.} \end{cases}$$

This allows the roots to get very close to the stone surface without the need to refine the mesh or increase the polynomial order of the repulsion function. The same repulsion function was imposed in the first layer of elements near the top surface of the domain to avoid the roots growing above the soil surface.

A detail on the behavior of the RSA in the surroundings of one of the stones is shown in Fig. 12. Finally, Fig. 13 provides an xy plane perspective of the final RSA, from the top and bottom faces of the computational domain.

The number of degrees of freedom involved in this numerical example tends to increase fast, as we are simulating the growth of the RSA for a quite long period of time, allowing for a high number of lateral roots. To enhance the efficiency of the proposed solving strategy we hence adopted a preconditioned conjugate gradient method to solve (66). In particular, we employed a simple



(a) $t = 40$ days (b) $t = 80$ days (c) $t = 160$ days

Fig. 11. TP3: RSA at three different time instants. Color scale refers to xylem pressure head.

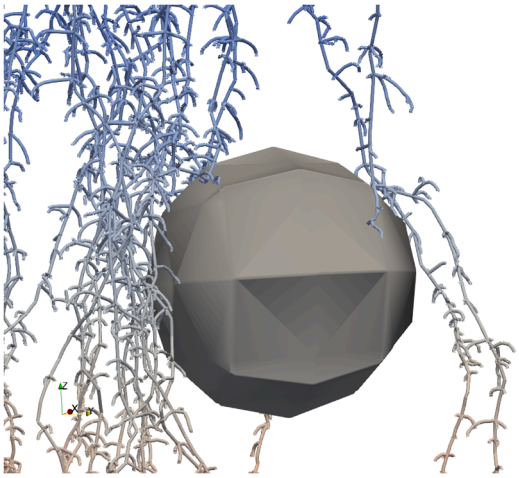
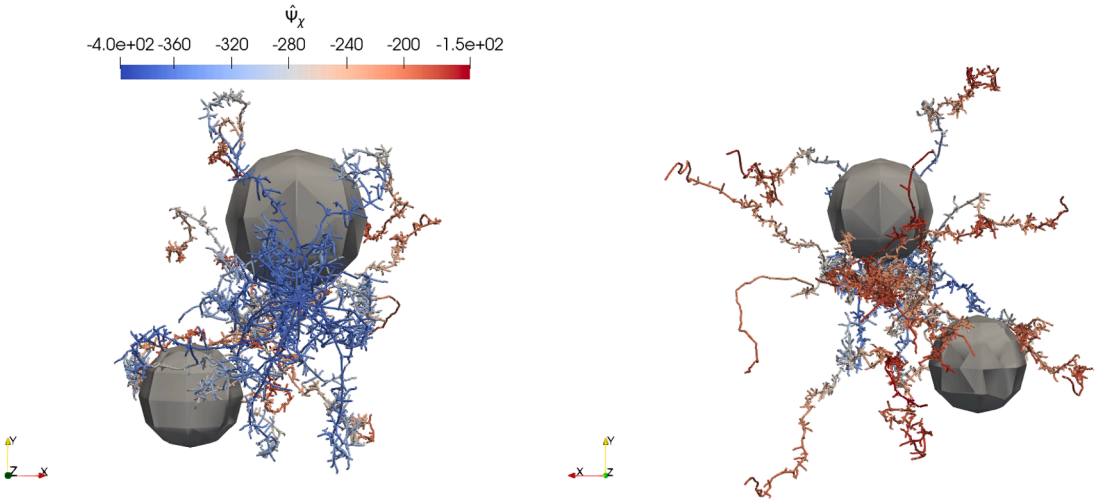


Fig. 12. TP3: detail of the RSA around a stone.



(a) $t = 160$ days, view from top face. (b) $t = 160$ days, view from bottom face.

Fig. 13. TP3: Top and bottom view of the RSA at $t = 160$ days.

Table 4
TP3: Number of iterations of the conjugate gradient scheme required at each non-linear step ℓ for 4 different time intervals ΔI_j. Non-preconditioned (no prec.) and preconditioned ($\boldsymbol{\mathcal{P}}$) case. The total number of DOFs for the control variables is also reported for each considered time-step.

j	1						5					10					15			
$\widehat{N}_\varsigma^\phi + \widehat{N}_\chi^\phi$	6						36					228					954			
ℓ	0	1	2	3	4	5	0	1	2	3	4	0	1	2	3	4	0	1	2	3
# CG (no prec.)	9	8	5	2	2	0	23	15	4	4	0	128	105	8	2	0	897	894	12	2
# CG ($\boldsymbol{\mathcal{P}}$)	4	4	3	2	0	0	5	4	3	2	1	7	4	3	1	0	8	5	4	0

preconditioner, defined as

$$\boldsymbol{\mathcal{P}} = \begin{bmatrix} \boldsymbol{G} & \boldsymbol{0} \\ \boldsymbol{0} & \widehat{\boldsymbol{G}} \end{bmatrix}. \tag{75}$$

where matrices $\boldsymbol{G}$ and $\widehat{\boldsymbol{G}}$ are the mass matrices related to soil and xylem control variables, respectively, that are involved in the diagonal blocks of matrix $\boldsymbol{\mathcal{M}}$ defined in (C.9). We refer to Appendix C for further details on the definition of these matrices. The proposed preconditioner can hence be seen as a very coarse approximation of matrix $\boldsymbol{\mathcal{M}}$, retaining only the blocks that do not require the inversion of any matrix. Table 4 shows the number of conjugate gradient iterations required, with and without preconditioning, for each iteration ℓ of the non-linear solver during 4 different timesteps ΔI_j, with $j = 1, 5, 10, 15$. We can observe that in both cases, and as observed also in TP1, the number of required CG iterations decreases from the first to the last non-linear iteration. However, in the non-preconditioned case, the number of CG iterations at the first non-linear steps tends to increase very rapidly with the number of degrees of freedom of the control variables ($\widehat{N}_\varsigma^\phi + \widehat{N}_\chi^\phi$). On the contrary, using the preconditioner $\boldsymbol{\mathcal{P}}$, the number of CG iterations tends to remain much lower and almost unchanged. It is interesting to remark that at the last considered time step, characterized by $\widehat{N}_\varsigma^\phi + \widehat{N}_\chi^\phi = 422978$ degrees of freedom for the control variables, the preconditioned algorithm still requires only 15, 11, 2 and 0 iterations of the conjugate gradient scheme respectively for the 4 non-linear steps performed. The non-preconditioned version was not pushed that far. For the sake of completeness, let us specify that the conjugate gradient iterations are stopped, for both the preconditioned and non-preconditioned case, when the norm of the absolute residual $r(\mathcal{X}) = \boldsymbol{\mathcal{M}}\mathcal{X} + \boldsymbol{d}$ goes under a certain threshold. In particular when

$$\|r(\mathcal{X})\| < 10^{-6}(1 + \|r(\mathcal{X}_0)\|).$$

At the beginning of each time step, after the RSA has been updated, the initial guess $\mathcal{X}_0$ on the new root network is computed by averaging the value of the control variables on the old network and by distributing this constant value on the whole new RSA, while at each non-linear step the initial guess is given by the value of the control variables produced at the previous non-linear step.

7. Conclusions

In this work we propose the application of an optimization-based 3D-1D coupling approach to the modeling and simulation of the exchanges between a soil sample and a growing root-network. In particular, we aim at computing the water pressure head in the soil and in the root-xylem, by coupling Richards equation in primal form in the soil domain with Stokes equation in the root xylem. An additional reaction term is included in the Stokes equation to account for the porous nature of the xylem tissue. Thanks to proper assumptions on the regularity of the quantities of interest, the root xylem is identified with the root centerline, leading to a well-posed 3D-1D reduced formulation of the problem. The Virtual Element Method is used to discretize the problem in the bulk soil domain, while Mixed Finite Elements are adopted to discretize the problem in the xylem. The imposition of coupling conditions at the soil-root interface is tackled by means of a PDE-constrained optimization approach, which ends up in a direct computation of interface quantities. The use of the VEM for the 3D discretization extends the applicability of the method to complex shaped computational domains, easing the meshing process in the presence of physical obstacles such as pot walls or stones. Root growth is modeled by means of a continuous- discrete hybrid tip-tracking strategy, endowed with proper rules for the emergence of lateral roots. The proposed approach is validated by several numerical examples, showing both the accuracy of the method and its applicability with an increasing number of degrees of freedom.

The discretization of Richards equation by Mixed Virtual Elements will be the subject of a forthcoming work, as well as a deeper investigation on the computational tools that may increase the efficiency of the solving strategy, such as tailored preconditioners and parallelization. Moreover, the design of effective strategies to handle the degeneracies that characterize the Richards equation within the virtual element framework, which are not addressed in the present work, will be the subject of upcoming research.

Data availability

Data will be made available on request.

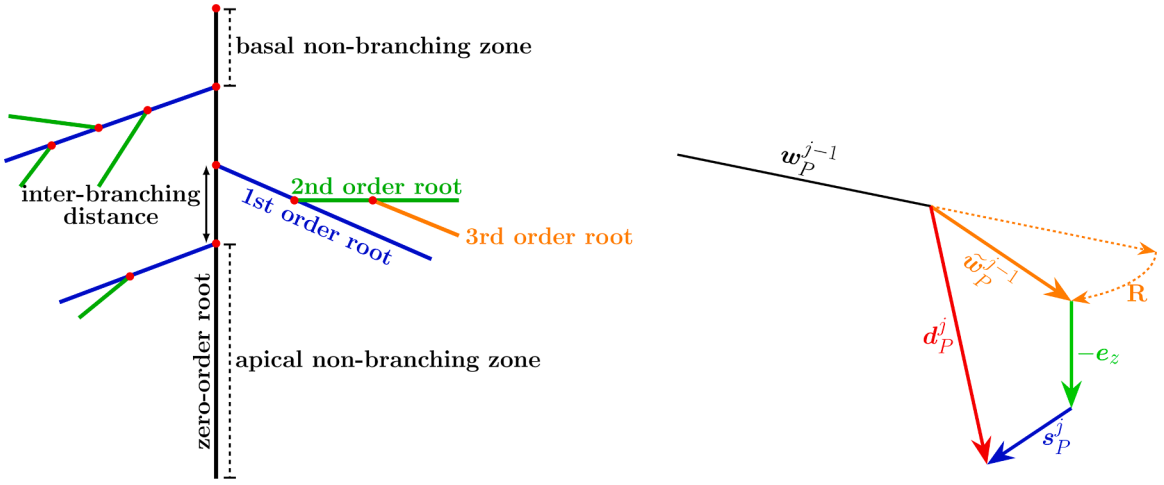
Declaration of competing interest

The authors declare no competing interests.

Acknowledgements

The author S.B. kindly acknowledges partial financial support provided by PNRR M4C2 project of CN00000013 National Centre for HPC, Big Data and Quantum Computing (HPC) (CUP: E13C22000990001) and the funding by the European Union through project Next Generation EU, M4C2, PRIN 2022 PNRR project P2022BH5CB_001 “Polyhedral Galerkin methods for engineering applications to improve disaster risk forecast and management: stabilization-free operator-preserving methods and optimal stabilization methods.”. The author S.F. kindly acknowledges partial financial support provided by Project NODES, which received funding from the MUR-M4C2 1.5 of the National Recovery and Resilience Plan (PNRR) with grant agreement no. ECS00000036 and by PRIN 2022 “202295PFKP - Snow droUghts predictioN in the Alps: a changing climate assessmEnT: SUNSET”. The author D.G. kindly acknowledges that this work was carried out while holding a postdoctoral fellowship financed by INdAM (Istituto Nazionale di Alta Matematica), hosted at the research unit of DISMA, Politecnico di Torino. The author G.T. kindly acknowledges financial support provided by the MIUR programme “Programma Operativo Nazionale Ricerca e Innovazione 2014 - 2020” (CUP: E11B21006490005) and by INdAM-GNCS Project “Metodi numerici efficienti per problemi accoppiati in sistemi complessi” (CUP: E53C24001950001). The author F.V. kindly acknowledges the financial support by INdAM-research group GNCS, project title: Metodi numerici avanzati per equazioni alle derivate parziali in fenomeni di trasporto e diffusione - (CUP: E53C24001950001).

Appendix A. Modeling root growth



(a) Nomenclature for the root system architecture. (b) Components of $\boldsymbol{d}_P^j$.

Fig. A.1. Nomenclature for root growth.

A root system may be seen as a set of axes, which are characterized by a ramification order: zero-order roots (or primary axes), which originate from the stem or the seed; first-order lateral roots, which are connected to the primary axes; second-order lateral roots, which are connected to the first-order lateral roots; and so forth [18] (see Fig. A.1a for a graphical illustration). The roots grow in an acropetal order, i.e., the youngest roots are the most lateral and closest to the apex. We always assume the seed to be in a known position and to be connected to the soil surface by a vertical mesocotyl [18].

Root growth is here modeled by a tip-tracking approach, providing a law for the evolution in time of the position of root tips, which is defined in (45). For ease of reading, we report here the definition of the growth field given in (68), namely

$$\boldsymbol{w}_P^j := V_P^j \frac{(1-\eta^2(\boldsymbol{x}_P))\boldsymbol{d}_P^j + \eta^2(\boldsymbol{x}_P)\boldsymbol{r}_P}{||(1-\eta^2(\boldsymbol{x}_P))\boldsymbol{d}_P^j + \eta^2(\boldsymbol{x}_P)\boldsymbol{r}_P||}, \quad \forall P \in \mathcal{P}_{\text{tip}}^{j-1} \quad \text{and} \quad j = 1, \dots, J, \tag{A.1}$$

where the repulsion function η and the direction $\boldsymbol{r}_P$ are defined in (67). The growth rate V_P^j employed to update the position $\boldsymbol{x}_P$ of the root tip $P \in \mathcal{P}_{\text{tip}}^{j-1}$, in the time interval $\mathcal{I}_j = (t_{j-1}, t_j]$ is defined as (see [20,61])

$$V_P^j = V_a(t_{j-1})\ \text{Imp}(\sigma(t_{j-1}, \boldsymbol{x}_P))\ \text{Imp}(\psi_\varsigma(t_{j-1}, \boldsymbol{x}_P)). \tag{A.2}$$

The maximum root elongation rate V_a [cm day^{-1}] can be a function of time through the root age, for example, whereas $\mathrm{Imp}(\sigma)$ and $\mathrm{Imp}(\psi_\varsigma)$ are dimensionless impedance factors modeling the impact of soil properties on the actual elongation rate. Let us introduce the soil-strength function $\sigma(t, \boldsymbol{x})$ ([MPa]), which can be defined empirically as [62]:

$$\sigma = \sigma_{\max}(1-\Theta)^3, \tag{A.3}$$

where $\sigma_{\max}$ [MPa] is a parameter that incorporates the effects of soil texture and bulk density and

$$\Theta = \frac{\theta - \theta_r}{\theta_s - \theta_r}$$

is the effective saturation, with θ_r and θ_s denoting the residual and the saturated volumetric water content, respectively. The soil-strength impedance factor $\mathrm{Imp}(\sigma)$ is then defined as

$$\mathrm{Imp}(\sigma) = \begin{cases} 0 & \text{if } \sigma \geq \sigma_{\max}, \\ 1 - \frac{\sigma}{\sigma_{\max}} & \text{if } \sigma < \sigma_{\max}, \end{cases} \tag{A.4}$$

where a reduced mechanical impedance results in faster elongation. Under non-optimal conditions related to a water deficit (drought) or poor aeration (hypoxia), the root elongation is reduced by means of the stress factor, depending on $\psi_\varsigma(t, \boldsymbol{x})$ [20,63]:

$$\mathrm{Imp}(\psi_\varsigma) = \begin{cases} 0 & \text{if } |\psi_\varsigma| \leq |(\psi_\varsigma)_1|, \\ \frac{|(\psi_\varsigma)_1| - |\psi_\varsigma|}{|(\psi_\varsigma)_1| - |(\psi_\varsigma)_2|} & \text{if } |(\psi_\varsigma)_1| < |\psi_\varsigma| \leq |(\psi_\varsigma)_2|, \\ 1 & \text{if } |(\psi_\varsigma)_2| < |\psi_\varsigma| \leq |(\psi_\varsigma)_3|, \\ \frac{|(\psi_\varsigma)_4| - |\psi_\varsigma|}{|(\psi_\varsigma)_4| - |(\psi_\varsigma)_3|} & \text{if } |(\psi_\varsigma)_3| < |\psi_\varsigma| \leq |(\psi_\varsigma)_4|, \\ 0 & \text{if } |\psi_\varsigma| > |(\psi_\varsigma)_4|. \end{cases} \tag{A.5}$$

The values $|(\psi_\varsigma)_1|$ and $|(\psi_\varsigma)_4|$ correspond to the hypoxia and drought thresholds, respectively, whereas the pressure head is assumed to be optimal for root growth between $|(\psi_\varsigma)_2|$ and $|(\psi_\varsigma)_3|$.

Other factors, such as temperature or nutrient concentration, can influence the root elongation rate [62,64]. However, for simplicity, we assume these factors to be constant and equal to their optimal values, thereby posing no impedance to root growth.

Concerning the growth direction $\boldsymbol{d}_P^j$ employed in (A.1), it is defined as

$$\boldsymbol{d}_P^j := \frac{k_s \boldsymbol{s}_P^j - k_g \boldsymbol{e}_z + k_w \widetilde{\boldsymbol{w}}_P^{j-1}}{\| k_s \boldsymbol{s}_P^j - k_g \boldsymbol{e}_z + k_w \widetilde{\boldsymbol{w}}_P^{j-1} \|}. \tag{A.6}$$

See Fig. A.1b for a graphical illustration. The vector field $\boldsymbol{s}_P^j$ accounts for mechanical constraints and it is defined as

$$\boldsymbol{s}_P^j = -\frac{\nabla\sigma(t_{j-1}, \boldsymbol{x}_P)}{\|\nabla\sigma(t_{j-1}, \boldsymbol{x}_P)\|}.$$

Since a higher soil water content results in lower soil strength, roots will tend to grow towards the wetter and hence less resistant soil regions. This tendency is called *hydrotropism*. The positive dimensionless parameter k_s in (A.6) allows to tune the weight of hydrotropism with respect to other tropisms: it can depend on the species, root order, and age.

The term $-k_g \boldsymbol{e}_z$ in (A.6) allows us to account for *geotropism*, which is the tendency of roots to grow downwards. The weight k_g is dimensionless and it may depend again on species, root age, and order.

Finally, the term $k_w \widetilde{\boldsymbol{w}}_P^{j-1}$ summarizes the plant roots tendency to preserve an already established growth direction (*exotropism*) while exploring the surrounding environment [15,62]. We set

$$\widetilde{\boldsymbol{w}}_P^{j-1} := \frac{\mathbf{R}\boldsymbol{w}_P^{j-1}}{\|\mathbf{R}\boldsymbol{w}_P^{j-1}\|}, \tag{A.7}$$

where matrix $\mathbf{R}$ is a random perturbation of the identity matrix $\mathbf{I}$ such that

$$\mathbf{R} = \mathbf{I} + m_a \begin{bmatrix} -m_2^2 - m_3^2 & m_1 m_2 & m_1 m_3 \\ m_1 m_2 & -m_1^2 - m_3^2 & m_2 m_3 \\ m_1 m_3 & m_2 m_3 & -m_1^2 - m_2^2 \end{bmatrix}.$$

The coefficients m_i, $i = 1, \ldots, 3$, normalized such that $\sum_{i=1}^3 m_i^2 = 1$, are randomly chosen in $[0, 1]$ according to a uniform distribution each time a growth direction is computed. The parameter m_a weighs how much the identity is actually perturbed, and it allows us to introduce some stochasticity in the root tip trajectory, taking into account the space-exploring nature of roots. As for the other types of tropism, the weight k_w is dimensionless and may depend on species, root age and order. The same matrix $\mathbf{R}$ was used in the tip-tracking strategy adopted in [57] to model the random orientation of extracellular matrix fibers in angiogenesis simulations.

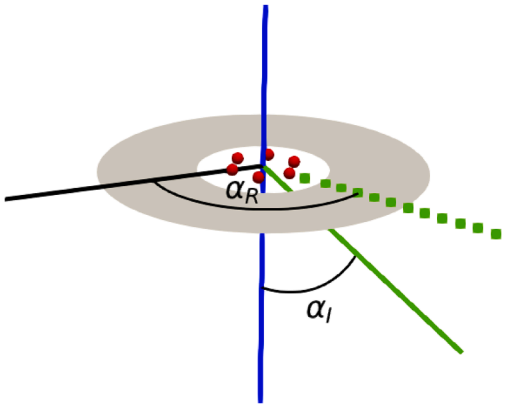


Fig. A.2. Branching angle and direction.

A.1. Branching

As the RSA grows, new zero-order roots can emerge, and existing roots can branch. The branching process can be split into two main steps: determining the branching position and the branching direction. Under normal conditions, no branching either occurs at some distance from the axis basis (the length of the basal non-branching zone L_B) or from the root tip (length of the apical non-branching zone L_A). For primary axes, the axis basis corresponds with the position of the seed; for secondary axis, not originating directly from the seed, the axis basis corresponds instead with the originating branching point on the parent axis. Potential branching nodes can arise between these two zones at regular intervals defined by an inter-branching distance I [18]. Let us denote by ℓ_P^{j-1} the length of a given root axis ending in a root tip $P \in \mathcal{P}_{\text{tip}}^{j-1}$. The maximum number of potential nodes at time t_{j-1} for the root axis ending in $\boldsymbol{x}_P$ is given by

$$N_b = \begin{cases} 0 & \text{if } \ell_P^j < L_A + L_B \\ \left\lfloor \dfrac{\ell_P^j - (L_A + L_B)}{I} \right\rfloor + 1 & \text{if } \ell_P^j \geq L_A + L_B. \end{cases}$$

At each time step, each of these potential branching sites may either develop into an emerged lateral root or remain unbranched, according to a Bernoulli distribution of probability p_{br} [18,65]. The sites from which a lateral root actually emerges in the time interval $\mathcal{I}_j$ are collected in $\mathcal{P}_{branch}^{j-1}$. As in [66], we model the probability p_{br} of generating a new branch from each potential node as a decreasing function of the order ω of the root on which the potential node is located. In particular, we set

$$p_{br}(\omega) = \begin{cases} \dfrac{e^{-b_c(\omega+1)}}{\sum_{i=0}^{\omega_{\max}} e^{-b_c(i+1)}} & \text{if } \omega = 0, \dots, \omega_{\max} - 1, \\ 0 & \text{if } \omega = \omega_{\max}. \end{cases} \tag{A.8}$$

For example, the root systems of agricultural plants like maize, wheat, etc. typically have $\omega_{\max} = 2$ or $\omega_{\max} = 3$ as maximum branching order [67]. If we choose $b_c \to 0$ branching becomes equiprobable at all potential nodes of all orders, while branching tends to be restricted to the nodes of the primary axes for bigger values of b_c. We remark that there are no potential nodes on roots of order $\omega_{\max}$. Of course, different choices for this branching probability function are possible. Also, different strategies to define potential nodes and to account for the emergence of branches from potential nodes can be adopted (see, for example, [68]).

The direction $\boldsymbol{b}_P^j$ of a branch sprouting from a point $P \in \mathcal{P}_{\text{branch}}^{j-1}$ during the time interval $\mathcal{I}_j$ is determined by two angles: an insertion angle $\alpha_I \in [0, \pi)$ and a radial angle $\alpha_R \in [0, 2\pi)$ [18,69]. The insertion angle α_I is defined as the angle between the parent root and the branch in the plane defined by these two axes. The radial angle α_R is defined as the angle between a given direction and the branch direction in the plane perpendicular to the parent root. It can be defined as

$$\alpha_R := \frac{2\pi N_R}{X},$$

where X is the number of xylem poles where new lateral roots emerge, which are assumed to be uniformly distributed, and N_R is a random integer number between 1 and X (see Fig. A.2 for a graphic illustration).

Finally, the growth field $\boldsymbol{w}_{P^\star}^j$ related to the new tip $P^\star \in \mathcal{P}_{\text{tip}}^j$ originating from $P \in \mathcal{P}_{\text{tip}}^{j-1}$ is computed as

$$\boldsymbol{w}_{P^\star}^j = V_{P^\star}^j \boldsymbol{b}_P^j,$$

and its position is determined by

$$\boldsymbol{x}_{P^\star}^j = \boldsymbol{x}_P^{j-1} + \Delta\mathcal{I}_j \boldsymbol{w}_{P^\star}^j.$$

Appendix B. Root growth parameters used in the simulations

We here provide the root growth parameters used in the test problems TP2 (Section 6.2) and TP3 (Section 6.3). In both test cases, we allow for a maximum of 3 root orders, $\omega \in \{0, 1, 2\}$.

B.1. Root growth parameters for TP2

For this test case we assume to be in optimal growth conditions: we set $\mathrm{Imp}(\psi_\varsigma) = 1$ for all the values of ψ_ς while, given the small pressure head absolute values, the soil strength impedance tends automatically to 1, according to (72), (A.3) and (A.4). In this simplified setting, we assume that the maximum root elongation rate V_a, defined in (A.2), is constant in time and that it depends only on the root order, i.e. we set

$$V_a(t) = \overline{V}_a(\omega) \quad \forall t.$$

The values of all the parameters related to root growth are reported in Table B.1.

Table B.1
TP2: RSA growth parameters used for simulation.

Parameter	Value			Unit	Description
	0	1	2		
$\overline{V}_a$	1	0.8	0.6	cm	Growth rate
L_B	0.8	0.8	–	cm	Length of basal non-branching zone
L_A	2	0.5	–	cm	Length of apical non-branching zone
I	1	0.4	–	cm	Inter-branch distance
α_I	1.4	1.2	–	rad	Branching insertion angle
X	5	3	–	–	Number of xylem poles
b_c	1	1	–	–	Branching probability parameter
k_g	0.1	0.1	0.1	–	Geotropism weight
k_s	0.25	0.25	0.25	–	Hydrotropism weight
k_w	1	1	1	–	Exotropism weight
m_a		[0,1]		–	Space exploration parameter

B.2. Root growth parameters for TP3

The parameters concerning the development of the RSA used in the TP3 Section 6.3 are reported in Table B.2. They are mostly taken from [70] and slightly adapted to the proposed growth model. Although most parameters refer to winter wheat, we underline that the primary aim of this numerical example is to test the viability of the proposed 3D-1D VEM approach on a simulation involving a larger number of degrees of freedom, regardless of the choice of the actual plant genotype. Some of the parameters reported in Table B.2 are stochastic and follow either a lognormal or a uniform distribution. In the first case we report the mean value and the standard deviation inside round brackets, whereas in the second we provide the bounds of the uniform distribution inside square brackets. Let us remark that most of the parameters vary with the root order. Those for which we report only a single value or the data of a single distribution are instead assumed to be invariant with respect to root order.

Unlike the previous test case, we allow for more than a zero-order root sprouting from the seed. At the initial time, we consider a single straight root segment Λ^0, representing the vertical mesocotyl. It is parallel to the z-axis and connects the seed with the top surface of the computational soil domain, as shown in Fig. 10a. From a computational standpoint, at the first time step the seed is assumed to be both an element of $\mathcal{P}^0_{\text{tip}}$ and of $\mathcal{P}^0_{\text{branch}}$, with $X = 19$ potential zero order root that can emerge and which are treated as if they were lateral branches of the vertical mesocotyl, emerging with probability $p_{br}(0)$ with a certain insertion and radial angle (see A.1). In the following time-steps, the seed keeps being an element of $\mathcal{P}^j_{\text{branch}}$, until the maximum number of sprouting roots is saturated. For what concerns root tips, we link their growth rate to root order and root age. In particular, we set

$$V_a(t_j) = \begin{cases} \overline{V}_a(0) & \text{if } \omega = 0 \\ \overline{V}_a(\omega) e^{-\frac{\overline{V}_a(\omega)}{L_{\max}(\omega)} a_P^j} & \text{if } \omega = 1, 2 \end{cases}$$

where a_P^j represents the age of the root ending in the tip P at time t_j and $L_{\max}$ is the maximum root elongation, depending on the order.

Table B.2
TP3: RSA growth parameters used for simulation. Stochastic parameters follow either a log-normal distribution characterized by *mean* (*standard deviation*) or a uniform distribution in [*lower bound*, *upper bound*] [70].

Parameter	Value			Unit	Description
	0	1	2		
$\lvert(\psi_\varsigma)_1\rvert$		1		cm	Hypoxia threshold
$\lvert(\psi_\varsigma)_2\rvert$		510		cm	Lower bound for $\mathrm{Imp}(\psi_\varsigma) = 1$
$\lvert(\psi_\varsigma)_3\rvert$		920		cm	Upper bound for $\mathrm{Imp}(\psi_\varsigma) = 1$
$\lvert(\psi_\varsigma)_4\rvert$		$1.6 \cdot 10^4$		cm	Drought threshold
$\overline{V}_a$	1.2 (0.6)	1 (0.2)	0.4 (0.12)	cm	Growth rate
L_B	0.8 (1.2)	0.8 (1)	–	cm	Length of basal non-branching zone
L_A	4.2 (6.4)	1.8 (2.4)	–	cm	Length of apical non-branching zone
I	0.8 (0.4)	1 (0.5)	–	cm	Inter-branch distance
α_I	1.4 (0.2)	1.2(0.4)	–	rad	Branching insertion angle
X	5	3	–	–	Number of xylem poles
b_c	1	1	–	–	Branching probability parameter
k_g		[0.1, 0.2]		–	Geotropism weight
k_s		[0.35, 0.45]		–	Hydrotropism weight
k_s	2	1	1	–	Exotropism weight
m_a		[0,1]		–	Space exploration parameter

Appendix C. Definition of the matrices involved in the solving strategy

To derive the algebraic form of the discrete cost functional (61), let us introduce the following matrices:

$$\widehat{\mathbf{M}} \in \mathbb{R}^{\widehat{N}_\chi^\psi \times \widehat{N}_\chi^\psi} : \qquad [\widehat{\mathbf{M}}]_{\alpha\beta} = \left(\widehat{\varphi}_{\chi,\beta}^\psi, \widehat{\varphi}_{\chi,\alpha}^\psi\right)_{\Lambda^j}, \tag{C.1}$$

$$\mathbf{M} \in \mathbb{R}^{N_\varsigma^\psi \times N_\varsigma^\psi} : \qquad [\mathbf{M}]_{\alpha\beta} = \left(\varphi_{\varsigma,\beta}^\psi, \varphi_{\varsigma,\alpha}^\psi\right)_{\Lambda^j}, \tag{C.2}$$

$$\widehat{\mathbf{G}} \in \mathbb{R}^{\widehat{N}_\varsigma^\phi \times \widehat{N}_\varsigma^\phi} : \qquad [\widehat{\mathbf{G}}]_{\alpha\beta} = \left(\widehat{\varphi}_{\chi,\beta}^\phi, \widehat{\varphi}_{\chi,\alpha}^\phi\right)_{\Lambda^j}, \tag{C.3}$$

$$\mathbf{G} \in \mathbb{R}^{\widehat{N}_\chi^\phi \times \widehat{N}_\chi^\phi} : \qquad [\mathbf{G}]_{\alpha\beta} = \left(\widehat{\varphi}_{\varsigma,\beta}^\phi, \widehat{\varphi}_{\varsigma,\alpha}^\phi\right)_{\Lambda^j}, \tag{C.4}$$

$$\mathbf{D}^\varsigma \in \mathbb{R}^{N_\varsigma^\psi \times \widehat{N}_\varsigma^\phi} : \qquad [\mathbf{D}^\varsigma]_{\alpha\beta} = \left(\varphi_{\varsigma,\alpha}^\psi, \widehat{\varphi}_{\varsigma,\beta}^\phi\right)_{\Lambda^j}, \tag{C.5}$$

$$\mathbf{D}^\chi \in \mathbb{R}^{\widehat{N}_\chi^\psi \times \widehat{N}_\chi^\phi} : \qquad [\mathbf{D}^\chi]_{\alpha\beta} = \left(\widehat{\varphi}_{\chi,\alpha}^\psi, \widehat{\varphi}_{\chi,\beta}^\phi\right)_{\Lambda^j}, \tag{C.6}$$

such that $\widetilde{\mathcal{J}}$ can be written in matrix form as

$$\widetilde{\mathcal{J}}(\widehat{\Phi}_\varsigma^n, \widehat{\Phi}_\chi^n) = \frac{1}{2}\left(\begin{bmatrix} \Psi_\varsigma^n(\widehat{\Phi}_\chi^n) \\ \widehat{\Psi}_\chi^n(\widehat{\Phi}_\varsigma^n) \\ \widehat{\Phi}_\varsigma^n \\ \widehat{\Phi}_\chi^n \end{bmatrix}^T \begin{bmatrix} \mathbf{M} & \mathbf{0} & -\mathbf{D}^\varsigma & \mathbf{0} \\ \mathbf{0} & \widehat{\mathbf{M}} & \mathbf{0} & -\mathbf{D}^\chi \\ -(\mathbf{D}^\varsigma)^T & \mathbf{0} & \mathbf{G} & \mathbf{0} \\ \mathbf{0} & -(\mathbf{D}^\chi)^T & \mathbf{0} & \widehat{\mathbf{G}} \end{bmatrix} \begin{bmatrix} \Psi_\varsigma^n(\widehat{\Phi}_\chi^n) \\ \widehat{\Psi}_\chi^n(\widehat{\Phi}_\varsigma^n) \\ \widehat{\Phi}_\varsigma^n \\ \widehat{\Phi}_\chi^n \end{bmatrix}\right). \tag{C.7}$$

Referring instead to the matrices introduced in Section 4.3, for the sake of compactness we define

$$\widehat{\mathcal{A}} = \begin{bmatrix} \widehat{\mathbf{A}} & \widehat{\mathbf{B}}^T \\ \widehat{\mathbf{B}} & -\widehat{\mathbf{M}}_\mu \end{bmatrix}, \quad \widehat{f} = \begin{bmatrix} \widehat{f}_\chi \\ \mathbf{0} \end{bmatrix},$$

so that according to (62)-(63) we have

$$\Psi_\varsigma^{n,\ell}(\widehat{\Phi}_\chi^{n,\ell}) = \left(\mathcal{A}^\ell\right)^{-1}\left(\mathbf{S}_\mu^\varsigma \widehat{\Phi}_\chi^{n,\ell} + \boldsymbol{f}^\ell\right), \quad \begin{bmatrix} \widehat{U}_\chi^{n,\ell}(\widehat{\Phi}_\varsigma^{n,\ell}) \\ \widehat{\Psi}_\chi^{n,\ell}(\widehat{\Phi}_\varsigma^{n,\ell}) \end{bmatrix} = \widehat{\mathcal{A}}^{-1}\left(\begin{bmatrix} \mathbf{0} \\ -\mathbf{S}_\mu^\chi \end{bmatrix} \widehat{\Phi}_\varsigma^{n,\ell} + \widehat{f}\right). \tag{C.8}$$

Substituting in the discrete cost functional (C.7) we obtain

$$\begin{aligned} \widetilde{\mathcal{J}}(\widehat{\Phi}_\varsigma^{n,\ell}, \widehat{\Phi}_{\chi,h}^{n,\ell}) = \frac{1}{2}\Big[& (\Psi_\varsigma^{n,\ell})^T \mathbf{M} \Psi_\varsigma^{n,\ell} - 2(\Psi_\varsigma^{n,\ell})^T \mathbf{D}^\varsigma \widehat{\Phi}_\varsigma^{n,\ell} + (\widehat{\Phi}_\varsigma^{n,\ell})^T \ \mathbf{G} \ \widehat{\Phi}_\varsigma^{n,\ell} + \\ & \begin{bmatrix} \widehat{U}_\chi^{n,\ell} \\ \widehat{\Psi}_\chi^{n,\ell} \end{bmatrix}^T \begin{bmatrix} \mathbf{0} & \mathbf{0} \\ \mathbf{0} & \widehat{\mathbf{M}} \end{bmatrix} \begin{bmatrix} \widehat{U}_\chi^{n,\ell} \\ \widehat{\Psi}_\chi^{n,\ell} \end{bmatrix} - 2 \begin{bmatrix} \widehat{U}_\chi^{n,\ell} \\ \widehat{\Psi}_\chi^{n,\ell} \end{bmatrix}^T \begin{bmatrix} \mathbf{0} \\ \mathbf{D}^\chi \end{bmatrix} \widehat{\Phi}_\chi^{n,\ell} + (\widehat{\Phi}_{\chi,h}^{n,\ell})^T \ \widehat{\mathbf{G}} \ \widehat{\Phi}_\chi^{n,\ell}, \Big] = \\ & = \frac{1}{2}\left(\mathcal{X}^T \mathcal{M} \mathcal{X} + 2\mathcal{X}^T \boldsymbol{d} + b\right). \end{aligned}$$

where $\mathcal{X} = \begin{bmatrix} \widehat{\Phi}_{\varsigma}^{n,\ell} \\ \widehat{\Phi}_{\chi}^{n,\ell} \end{bmatrix}$ and

$$\mathcal{M} = \begin{bmatrix} \mathbf{G} + \begin{bmatrix} \mathbf{0} \\ -\mathbf{S}_{\mu}^{\chi} \end{bmatrix}^T (\widehat{\mathcal{A}})^{-1} \begin{bmatrix} \mathbf{0} & \mathbf{0} \\ \mathbf{0} & \widehat{\mathbf{M}} \end{bmatrix} (\widehat{\mathcal{A}})^{-1} \begin{bmatrix} \mathbf{0} \\ -\mathbf{S}_{\mu}^{\chi} \end{bmatrix} & -(\mathbf{D}^{\varsigma})^T (\mathcal{A}^{\ell})^{-1} \mathbf{S}_{\mu}^{\varsigma} - \begin{bmatrix} \mathbf{0} \\ -\mathbf{S}_{\mu}^{\chi} \end{bmatrix}^T (\widehat{\mathcal{A}})^{-1} \begin{bmatrix} \mathbf{0} \\ \mathbf{D}^{\chi} \end{bmatrix} \\ -(\mathbf{S}_{\mu}^{\varsigma})^T (\mathcal{A}^{\ell})^{-1} \mathbf{D}^{\varsigma} - \begin{bmatrix} \mathbf{0} \\ \mathbf{D}^{\chi} \end{bmatrix}^T (\widehat{\mathcal{A}})^{-1} \begin{bmatrix} \mathbf{0} \\ -\mathbf{S}_{\mu}^{\chi} \end{bmatrix} & \widehat{\mathbf{G}} + (\mathbf{S}_{\mu}^{\varsigma})^T (\mathcal{A}^{\ell})^{-1} \mathbf{M} (\mathcal{A}^{\ell})^{-1} \mathbf{S}_{\mu}^{\varsigma} \end{bmatrix}, \tag{C.9}$$

$$\boldsymbol{d} = \begin{bmatrix} -(\mathbf{D}^{\varsigma})^T (\mathcal{A}^{\ell})^{-1} \boldsymbol{f}^{\ell} + \begin{bmatrix} \mathbf{0} \\ -\mathbf{S}_{\mu}^{\chi} \end{bmatrix}^T (\widehat{\mathcal{A}})^{-1} \begin{bmatrix} \mathbf{0} & \mathbf{0} \\ \mathbf{0} & \widehat{\mathbf{M}} \end{bmatrix} (\widehat{\mathcal{A}})^{-1} \widehat{\boldsymbol{f}} \\ -\begin{bmatrix} \mathbf{0} \\ \mathbf{D}^{\chi} \end{bmatrix}^T (\widehat{\mathcal{A}})^{-1} \widehat{\boldsymbol{f}} + (\mathbf{S}_{\mu}^{\varsigma})^T (\mathcal{A}^{\ell})^{-1} \mathbf{M} (\mathcal{A}^{\ell})^{-1} \boldsymbol{f}^{\ell} \end{bmatrix}, \tag{C.10}$$

$$b = (\boldsymbol{f}^{\ell})^T (\mathcal{A}^{\ell})^{-1} \mathbf{M} (\mathcal{A}^{\ell})^{-1} \boldsymbol{f}^{\ell} + (\widehat{\boldsymbol{f}})^T (\widehat{\mathcal{A}})^{-1} \begin{bmatrix} \mathbf{0} & \mathbf{0} \\ \mathbf{0} & \widehat{\mathbf{M}} \end{bmatrix} (\widehat{\mathcal{A}})^{-1} \widehat{\boldsymbol{f}}. \tag{C.11}$$

Let us remark that the solving strategy summarized in Algorithm 1 can be applied without building explicitly matrix $\mathcal{M}$. Indeed, given a descent direction $\delta\mathcal{X}$ it is possible to prove that

$$\mathcal{M}\delta\mathcal{X} = \begin{bmatrix} \mathbf{G}\ \delta\widehat{\Phi}_{\varsigma} - (\mathbf{D}^{\varsigma})^T \delta\Psi_{\varsigma} - (\mathbf{S}_{\mu}^{\chi})^T \delta\widehat{P}_{\chi} \\ \widehat{\mathbf{G}}\ \delta\widehat{\Phi}_{\chi} - (\mathbf{D}^{\chi})^T \delta\widehat{\Psi}_{\chi} + (\mathbf{S}_{\mu}^{\varsigma})^T \delta P_{\varsigma} \end{bmatrix},$$

where $\delta\Psi_{\varsigma} \in \mathbb{R}^{N_{\varsigma}^{\psi}}$ and $\delta\widehat{\Psi}_{\chi} \in \mathbb{R}^{\widehat{N}_{\chi}^{\psi}}$ are the solutions of

$$\mathcal{A}^{\ell}\delta\Psi_{\varsigma} = \mathbf{S}_{\mu}^{\varsigma}\delta\widehat{\Phi}_{\chi}, \qquad \widehat{\mathcal{A}}\begin{bmatrix} \delta\widehat{U}_{\chi} \\ \delta\widehat{\Psi}_{\chi} \end{bmatrix} = \begin{bmatrix} \mathbf{0} \\ -\mathbf{S}_{\mu}^{\chi}\ \delta\widehat{\Phi}_{\varsigma} \end{bmatrix},$$

with $\delta\widehat{U}_{\chi} \in \mathbb{R}^{\widehat{N}_{\chi}^{u}}$. Similarly, $\delta P_{\varsigma} \in \mathbb{R}^{N_{\varsigma}^{\psi}}$, and $\delta\widehat{P}_{\chi} \in \mathbb{R}^{\widehat{N}_{\chi}^{\psi}}$ are the solutions of

$$\mathcal{A}^{\ell}\delta P_{\varsigma}^{n,\ell} = \mathbf{M}\delta\Psi_{\varsigma}^{n,\ell} - \mathbf{D}^{\varsigma}\delta\widehat{\Phi}_{\varsigma}^{n,\ell}, \quad \widehat{\mathcal{A}}\begin{bmatrix} \delta\widehat{W}_{\chi}^{n,\ell} \\ \delta\widehat{P}_{\chi}^{n,\ell} \end{bmatrix} = \begin{bmatrix} \mathbf{0} \\ \widehat{\mathbf{M}}\ \delta\widehat{\Psi}_{\chi}^{n,\ell} - \mathbf{D}^{\chi}\ \delta\widehat{\Phi}_{\chi}^{n,\ell} \end{bmatrix},$$

with $\delta\widehat{W}_{\chi} \in \mathbb{R}^{\widehat{N}_{\chi}^{u}}$.

References

[1] H. Vereecken, W. Amelung, S. Bauke, H. Bogena, N. Brüggemann, C. Montzka, J. Vanderborght, M. Bechtold, G. Blöschl, A. Carminati, M. Javaux, A. Konings, J. Kusche, I. Neuweiler, D. Or, S. Steele-Dunne, A. Verhoef, M. Young, Y. Zhang, Soil hydrology in the earth system, Nature Rev. Earth Environ. 3 (2022) 573–587. https://doi.org/10.1038/s43017-022-00324-6

[2] D. Vetterlein, M. Phalempin, E. Lippold, S. Schlüter, S. Schreiter, M.A. Ahmed, A. Carminati, P. Duddek, H. Jorda, G.P. Bienert, M.D. Bienert, M. Tarkka, M. Ganther, E. Oburger, M. Santangeli, M. Javaux, J. Vanderborght, Root hairs matter at field scale for maize shoot growth and nutrient uptake, but root trait plasticity is primarily triggered by texture and drought, Plant Soil 478 (1–2) (2022) 119 - 141. https://doi.org/10.1007/s11104-022-05434-0

[3] A. Schnepf, A. Carminati, M.A. Ahmed, M. Ani, P. Benard, J. Bentz, M. Bonkowski, M. Knott, D. Diehl, P. Duddek, E. Kröner, M. Javaux, M. Landl, E. Lehndorff, E. Lippold, A. Lieu, C.W. Mueller, E. Oburger, W. Otten, X. Portell, M. Phalempin, A. Prechtel, R. Schulz, J. Vanderborght, D. Vetterlein, Linking rhizosphere processes across scales: opinion, Plant Soil 478 (1–2) (2022) 5 - 42. https://doi.org/10.1007/s11104-022-05306-7

[4] A. Schnepf, D. Leitner, G. Bodner, M. Javaux, Editorial: benchmarking 3D-models of root growth, architecture and functioning, Front. Plant Sci. 13 (2022). https://doi.org/10.3389/fpls.2022.902587

[5] J. Vanderborght, D. Leitner, A. Schnepf, V. Couvreur, H. Vereecken, M. Javaux, Combining root and soil hydraulics in macroscopic representations of root water uptake, Vadose Zone J. 23 (3) (2024) e20273. https://doi.org/10.1002/vzj2.20273

[6] J. Vanderborght, V. Couvreur, M. Javaux, D. Leitner, A. Schnepf, H. Vereecken, Mechanistically derived macroscopic root water uptake functions: the α and ω of root water uptake functions, Vadose Zone J. 23 (4) (2024) e20333. https://doi.org/10.1002/vzj2.20333

[7] S.P. Ganesan, D. Boldrin, A.K. Leung, A closer look at root water potential: experimental evidence based on drought stress of chrysopogon zizanioides, Plant Soil 499 (2024) 569–585. https://doi.org/10.1007/s11104-024-06481-5

[8] W. Jin, J. Aufrecht, F. Patino-Ramirez, H. Cabral, C. Arson, S.T. Retterer, Modeling root system growth around obstacles, Sci. Rep. 10 (2020). https://doi.org/10.1038/s41598-020-72557-8

[9] M. Bordoni, V. Vivaldi, A. Giarola, R. Valentino, M. Bittelli, C. Meisina, Comparison between mechanical and hydrological reinforcement effects of cultivated plants on shallow slope stability, Sci. Total Environ. 912 (2024) 168999. https://doi.org/10.1016/j.scitotenv.2023.168999

[10] L. Beirão da Veiga, F. Brezzi, A. Cangiani, G. Manzini, A. Russo, Basic principles of virtual element methods, Math. Models Methods Appl. Sci. 23 (01) (2013) 199–214. https://doi.org/10.1142/S0218202512500492

[11] L. Beirão da Veiga, F. Brezzi, L.D. Marini, A. Russo, Virtual element method for general second-order elliptic problems on polygonal meshes, Math. Models Methods Appl. Sci. 26 (04) (2016) 729–750. https://doi.org/10.1142/S0218202516500160

[12] D. Adak, G. Manzini, S. Natarajan, The Mixed Virtual Element Method for the Richards Equation, 2020, pp. 223–257. https://doi.org/10.1007/978-3-030-69363-3_7

[13] G. Manzini, S. Ferraris, Mass-conservative finite volume methods on 2-D unstructured grids for the Richards' equation, Adv. Water Resour. 27 (12) (2004) 1199–1215. https://doi.org/10.1016/j.advwatres.2004.08.008

[14] S. Morandage, J. Vanderborght, M. Zörner, G. Cai, D. Leitner, H. Vereecken, A. Schnepf, Root architecture development in stony soils, Vadose Zone J. 20 (4) (2021) e20133. https://doi.org/10.1002/vzj2.20133

[15] T. Koch, K. Heck, N. Schröder, H. Class, R. Helmig, A new simulation framework for soil-root interaction, evaporation, root growth, and solute transport, Vadose Zone J. 17 (1) (2018) 170210. https://doi.org/10.2136/vzj2017.12.0210

[16] S. Berrone, D. Fassino, F. Vicini, 3D Adaptive VEM with stabilization-free a posteriori error bounds, J. Sci. Comput. 103 (1) (2025) 35. https://doi.org/10.1007/s10915-025-02852-x
[17] S. Berrone, F. Vicini, Effective polygonal mesh generation and refinement for VEM, Math. Comput. Simul. 231 (2025) 239–258. https://doi.org/https://doi.org/10.1016/j.matcom.2024.12.007
[18] L. Pagès, M.-O. Jordan, D. Picard, A simulation model of the three-dimensional architecture of the maize root system, Plant Soil 119 (1989) 147–154. https://doi.org/10.1007/BF02370279
[19] V.M. Dunbabin, J.A. Postma, A. Schnepf, L. Pagès, M. Javaux, L. Wu, D. Leitner, Y.L. Chen, Z. Rengel, A.J. Diggle, Modelling root-soil interactions using three-dimensional models of root growth, architecture and function, Plant Soil 372 (2013) 9–124. https://doi.org/10.1007/s11104-013-1769-y
[20] M.T. de Moraes, A.G. Bengough, H. Debiasi, J.C. Franchini, R. Levien, A. Schnepf, D. Leitner, Mechanistic framework to link root growth models with weather and soil physical properties, including example applications to soybean growth in Brazil, Plant Soil 428 (2018). https://doi.org/10.1007/s11104-018-3656-z
[21] A. Schnepf, C.K. Black, V. Couvreur, B.M. Delory, C. Doussan, A. Koch, T. Koch, M. Javaux, M. Landl, D. Leitner, G. Lobet, T.H. Mai, F. Meunier, L. Petrich, J.A. Postma, E. Priesack, V. Schmidt, J. Vanderborght, H. Vereecken, M. Weber, Call for participation: collaborative benchmarking of functional-Structural root architecture models. the case of root water uptake, Front. Plant Sci. 11 (2020). https://doi.org/10.3389/fpls.2020.00316
[22] A. Schnepf, C.K. Black, V. Couvreur, B.M. Delory, C. Doussan, A. Heymans, M. Javaux, D. Khare, A. Koch, T. Koch, C.W. Kuppe, M. Landl, D. Leitner, G. Lobet, F. Meunier, J.A. Postma, E.D. Schäfer, T. Selzner, J. Vanderborght, H. Vereecken, Collaborative benchmarking of functional-structural root architecture models: quantitative comparison of simulated root water uptake, Silico Plants 5 (1) (2023). https://doi.org/10.1093/insilicoplants/diad005
[23] S. Berrone, A. Borio, G. Teora, F. Vicini, POLYDIM: a C++ library for POLYtopal DIscretization methods, Comput. Phys. Commun. 320 (2026) 109937. https://doi.org/10.1016/j.cpc.2025.109937
[24] M.A. Celia, E.T. Bouloutas, R.L. Zarba, A general mass-conservative numerical solution for the unsaturated flow equation, Water Resour. Res. 26 (1990) 1483–1496. https://doi.org/10.1029/WR026i007p01483
[25] C. Scudeler, C. Paniconi, D. Pasetto, M. Putti, Examination of the seepage face boundary condition in subsurface and coupled surface/subsurface hydrological models, Water Resour. Res. 53 (3) (2017) 1799–1819. https://doi.org/10.1002/2016WR019277
[26] M.T. van Genuchten, A closed-form equation for predicting the hydraulic conductivity of unsaturated soils, Soil Sci. Soc. Am. J. 44 (5) (1980) 892–898. https://doi.org/10.2136/sssaj1980.03615995004400050002x
[27] K. Mitra, M. Vohralík, A posteriori error estimates for the Richards equation, Math. Comput. 93 (347) (2024) 1053 - 1096. https://doi.org/10.1090/mcom/3932
[28] R.H. Rand, J.R. Cooke, Fluid mechanics in plant biology, in: Handbook of Fluid Dynamics and Fluid Machinery, 3, 1996, pp. 1921–1938. https://doi.org/10.1002/9780470172650.ch24
[29] D. Notaro, L. Cattaneo, L. Formaggia, A. Scotti, P. Zunino, A Mixed Finite Element Method for Modeling the Fluid Exchange Between Microcirculation and Tissue Interstitium, Springer International Publishing, Cham, 2016, pp. 3–25. https://doi.org/10.1007/978-3-319-41246-7_1
[30] G. Vacca, An H1-conforming virtual element for Darcy and Brinkman equations, Math. Models Methods Appl. Sci. 28 (01) (2018) 159–194. https://doi.org/10.1142/S0218202518500057
[31] T.H. Mai, A. Schnepf, H. Vereecken, J. Vanderborght, Continuum multiscale model of root water and nutrient uptake from soil with explicit consideration of the 3D root architecture and the rhizosphere gradients, Plant Soil 439 (2019) 273–292. https://doi.org/10.1007/s11104-018-3890-4
[32] L. Cattaneo, P. Zunino, Computational models for fluid exchange between microcirculation and tissue interstitium, Netw. Heterogeneous Med. 9 (1) (2014) 135–159. https://doi.org/10.3934/nhm.2014.9.135
[33] N. Carro, D. Mora, J. Vellojin, A finite element model for concentration polarization and osmotic effects in a membrane channel, Int. J. Numer. Methods Fluids 96 (5) (2024) 601–625. https://doi.org/10.1002/fld.5252
[34] C. D'Angelo, Finite element approximation of elliptic problems with Dirac measure terms in weighted spaces: applications to one- and three-dimensional coupled problems, SIAM J. Numer. Anal. 50 (1) (2012) 194–215. https://doi.org/10.1137/100813853
[35] C. D'Angelo, A. Scotti, A mixed finite element method for Darcy flow in fractured porous media with non-matching grids, ESAIM: M2AN 46 (2) (2012) 465–489. https://doi.org/10.1051/m2an/2011148
[36] A.-K. Tornberg, B. Engquist, Numerical approximations of singular source terms in differential equations, J. Comput. Phys. 200 (2) (2004) 462–488. https://doi.org/10.1016/j.jcp.2004.04.011
[37] L. Heltai, A. Caiazzo, Multiscale modeling of vascularized tissues via nonmatching immersed methods, Int. J. Numer. Method Biomed. Eng. 35 (12) (2019) e3264. e3264 cnm.3264. https://doi.org/10.1002/cnm.3264
[38] T. Koch, M. Schneider, R. Helmig, P. Jenny, Modeling tissue perfusion in terms of 1d-3d embedded mixed-dimension coupled problems with distributed sources, J. Comput. Phys. 410 (2020) 109370. https://doi.org/10.1016/j.jcp.2020.109370
[39] I.G. Gjerde, K. Kumar, J.M. Nordbotten, Well modelling by means of coupled 1D-3D flow models, 2018. https://doi.org/10.3997/2214-4609.201802117
[40] I.G. Gjerde, K. Kumar, J.M. Nordbotten, B. Wohlmuth, Splitting method for elliptic equations with line sources, ESAIM: M2AN 53 (5) (2019) 1715–1739. https://doi.org/10.1051/m2an/2019027
[41] F. Laurino, P. Zunino, Derivation and analysis of coupled PDEs on manifolds with high dimensionality gap arising from topological model reduction, ESAIM: M2AN 53 (6) (2019) 2047–2080. https://doi.org/10.1051/m2an/2019042
[42] M. Kuchta, F. Laurino, K.-A. Mardal, P. Zunino, Analysis and approximation of mixed-dimensional PDEs on 3D-1D domains coupled with lagrange multipliers, SIAM J. Numer. Ana.l 59 (1) (2021) 558–582. https://doi.org/10.1137/20M1329664
[43] S. Berrone, D. Grappein, S. Scialò, A PDE-constrained optimization method for 3D-1D coupled problems with discontinuous solutions, Numer. Algorithms 95 (2024) 499–526. https://doi.org/10.1007/s11075-023-01579-w
[44] L. Formaggia, A. Veneziani, Reduced and multiscale models for the human cardiovascular system, Tech. Rep. PoliMI, Milan (2003). https://doi.org/10.13140/RG.2.1.3668.8088
[45] E. Peter, A. Bala, Application of Navier - Stokes equation to solve fluid flow problems, J. Adv. Math. Comput. Sci. (2020) 101–114. https://doi.org/10.9734/jamcs/2020/v35i830318
[46] S. Berrone, D. Grappein, S. Scialò, 3D-1D coupling on non conforming meshes via a three-field optimization based domain decomposition, J. Comput. Phys. 448 (2022) 110738. https://doi.org/10.1016/j.jcp.2021.110738
[47] K.B. Nakshatrala, M.S. Joshaghani, On interface conditions for flows in coupled free-Porous media, Transp. Porous Media 130 (2019) 577–609. https://doi.org/10.1007/s11242-019-01326-7
[48] L. Pagès, Root system architecture: from its representation to the study of its elaboration, Agronomie 19 (1999) 295–304. https://doi.org/10.1051/agro:19990309
[49] L. Beirão da Veiga, F. Dassi, A. Russo, High-order virtual element method on polyhedral meshes, Comput. Math. Appl. 74 (5) (2017) 1110–1122. SI: SDS2016 - Methods for PDEs. https://doi.org/10.1016/j.camwa.2017.03.021
[50] L. Beirão da Veiga, F. Brezzi, L. Marini, A. Russo, The Hitchhiker's guide to the virtual element method, Math. Models Methods Appl. Sci. 24 (8) (2014) 1541–1573. https://doi.org/10.1142/S021820251440003X
[51] S. Berrone, G. Teora, F. Vicini, Improving high-order VEM stability on badly-shaped elements, Math. Comput. Simul. 216 (2024) 367–385. https://doi.org/10.1016/j.matcom.2023.10.003
[52] A. Cangiani, P. Chatzipantelidis, G. Diwan, E.H. Georgoulis, Virtual element method for quasilinear elliptic problems, IMA J. Numer. Anal. 40 (4) (2019) 2450–2472. https://doi.org/10.1093/imanum/drz035
[53] G. Vacca, L. Beirão da Veiga, Virtual element methods for parabolic problems on polygonal meshes, Numer. Methods Partial Differ. Equ 31 (6) (2015) 2110–2134. https://doi.org/10.1002/num.21982
[54] F. List, F.A. Radu, A study on iterative methods for solving richards' equation, Comput. Geosci. 20 (2016) 341–353. https://doi.org/10.1007/s10596-016-9566-3
[55] S. Berrone, M. Pintore, G. Teora, The lowest-order neural approximated virtual element method on polygonal elements, Comput. Struct. 314 (2025) 107753. https://doi.org/10.1016/j.compstruc.2025.107753
[56] V.M. Dunbabin, M. Airey, A.J. Diggle, M. Renton, Z. Rengel, R. Armstrong, Y. Chen, K. Siddique, Simulating the interaction between plant roots, soil water

and nutrient flows, and barriers and objects in soil using ROOTMAP, F. Chan, D. Marinova, & R.S.Anderssen (Eds.), MODSIM2011, 19th International Congress on Modelling and Simulation, Modelling and Simulation Society of Australia and New Zealand (2011) 975–981. https://doi.org/10.36334/modsim.2011.B3.dunbabin

[57] S. Berrone, C. Giverso, D. Grappein, L. Preziosi, S. Scialò, An optimization based 3D-1D coupling strategy for tissue perfusion and chemical transport during tumor-induced angiogenesis, Comput. Math. Appl. 151 (2023) 252–270. https://doi.org/10.1016/j.camwa.2023.09.046

[58] M. Javaux, T. Schröder, J. Vanderborght, H. Vereecken, Use of a three-dimensional detailed modeling approach for predicting root water uptake, Vadose Zone J. 7 (3) (2008) 1079–1088. https://doi.org/10.2136/vzj2007.0115

[59] I.F. Cuneo, T. Knipfer, P. Mandal, C.R. Brodersen, A.J. McElrone, Water uptake can occur through woody portions of roots and facilitates localized embolism repair in grapevine, New Phytol. 218 (2) (2018) 506–516. https://doi.org/10.1111/nph.15032

[60] R.F. Carsel, R.S. Parrish, Developing joint probability distributions of soil water retention characteristics, Water Resour. Res. 24 (5) (1988) 755–769. https://doi.org/10.1029/WR024i005p00755

[61] S.J. Seidel, T. Gaiser, A.K. Srivastava, D. Leitner, O. Schmittmann, M. Athmann, T. Kautz, J. Guigue, F. Ewert, A. Schnepf, Simulating root growth as a function of soil strength and yield with a field-Scale crop model coupled with a 3D architectural root model, Front. Plant Sci. 13 (2022). https://doi.org/10.3389/fpls.2022.865188

[62] V. Clausnitzer, J.W. Hopmans, Simultaneous modeling of transient three-dimensional root growth and soil water flow, Plant Soil 164 (1994) 299–314. https://doi.org/10.1007/BF00010082

[63] R.A. Feddes, Simulation of Field Water Use and Crop Yield, simulation monographs, Pudoc, 1982, pp. 194–209.

[64] L. Wu, M.B. McGechan, C. Watson, J. Baddeley, Developing existing plant root system architecture models to meet future agricultural challenges, Adv. Agronomy 85 (2005) 181–219. https://doi.org/10.1016/S0065-2113(04)85004-1

[65] L. Pagès, Analysis and modeling of the variations of root branching density within individual plants and among species, Front Plant Sci 10 (2019). https://doi.org/10.3389/fpls.2019.01020

[66] A.H. Fitter, An architectural approach to the comparative ecology of plant root systems, New Phytol. 106 (1) (1987) 61–77. https://doi.org/10.1111/j.1469-8137.1987.tb04683.x

[67] T. Roose, A.C. Fowler, A mathematical model for water and nutrient uptake by plant root systems, J. Theor. Biol. 228 (2) (2004) 173–184. https://doi.org/10.1016/j.jtbi.2003.12.013

[68] C. Ziegler, R.J. Dyson, I.G. Johnston, Model selection and parameter estimation for root architecture models using likelihood-free inference, J. R. Soc. Interface 16 (156) (2019) 20190293. https://doi.org/10.1098/rsif.2019.0293

[69] A.H. Fitter, T.R. Stickland, M.L. Harvey, G.W. Wilson, Architectural analysis of plant root systems 1. architectural correlates of exploitation efficiency, New Phytol. 118 (3) (1991) 375–382. https://doi.org/10.1111/j.1469-8137.1991.tb00018.x

[70] S. Morandage, A. Schnepf, D. Leitner, M. Javaux, H. Vereecken, J. Vanderborght, Parameter sensitivity analysis of a root system architecture model based on virtual field sampling, Plant Soil 438 (2019) 101–126. https://doi.org/10.1007/s11104-019-03993-3